MPHIL

Sol-gel Optical Fibre

Dong, Tianqi

Award date:
2013

Awarding institution:
University of Bath

Sol-gel and optical fibre

Tianqi Dong

A thesis submitted for the degree of Master of Philosophy

University of Bath

Department of Physics

September 2013

Acknowledgements

I would like to express my most sincere gratitude to my supervisor Prof. Tim Birks for his continued guidance, advice and support.

For the people who help me, I thank wholeheartedly: Paul and Wendy, for their helpful machine work and chemical instruction; the one-year aerogel team at Bath, William, Richard, Mat, Limin and Michael; Brian, for fabricating aerogel fibre; Yong, for blocking aeogel fibre; Yuli, for providing Elliposometer at Department of Chemistry; Bob and Robert, for proof reading this thesis; other colleague and friends at University of Bath.

Studying aboard is very challenge for international students. During these three years I learned to deal with homesick and loneliness. Thanks for my lovely family, my parents and little brother I know you are always there and the piano in Bath Royal Literary and Scientific Institution (BRLSI), that accompanied with me and comforted me. Thanks Bob again, for recommending me BRLSI, where I heard lots of interesting scientific researches.

England is a nice country to live in and it cultures many great scientists. I feel very lucky to have the chance to keep a close eye to the culture and people here. Life in Bath is and will be an unforgettable memory in my life for the spirit and story.

Abstract

The aim of thesis is to explore the possible effects of sol-gel on the performance of fibre optics. It mainly contains three parts of the work. The first part was to fill designed fibres that have only single claddings with aerogel in the centre core. The aerogel core acted as an optical waveguide and the near field patterns of light in aerogel were observed, which showed that the light could be guided in the infrared region by total internal reflection. This phenomenon was in conformity with the theoretical analysis. The second part of work was to fabricate a thin layer crack-free silica film coated fibres after an aging process in methanol atmosphere for 12h with a thickness of approximately 600nm. A comparative refractive index of 1.30 was measured by depositing a thin film on a silica plan glass using the same procedure. The third part of the work was an extension of the second part, which was to form a silica thin film around tapers to control the distance between two tapers that dominated the coupling efficiency. The experimental designs of these three experiments were proposed, along with the results discussed, especially the positive filling design that would provide an efficient way of filling dopants in hollow core fibres.

List of acronyms

CCD	Charge-Coupled Device
InGaAs	Indium-Gallium-Arsenide
NA	Numerical Aperture
SCD	Supercritical Drying
SEM	Scanning Electron Microscopy
SMF	Single Mode Fibre
TEM	Transmission Electron Microscopy
TIR	Total Internal Reflection
HMDS	Haxamethyldisilazane
MTMS	Methytrimethoxysilane
TEOS	Tetraethoxysilane
TMOS	Tetramethoxysilane
TMS	Trimethylsilyl

CONTENTS

Chapter 1 Introduction

The aim of this research project is to utilise the sol-gel process in fibre optics to reveal possible interesting behaviour in the application. Sol-gel is a state-of-the-art method for producing solid materials from small particles, especially for glass [1]; fibre optic is one of the major technical breakthroughs of the last century that led to a revolution in communication [2]. In this thesis, sol-gel technique is investigated in research specifically concerning the filling of a hollow core with aerogel as well as the fabrication of a uniform, crack-free thin film coating applied to a fibre. A combination of these innovative fibre fabrication techniques should boost the performance of current fibres and it should pave the way to many potential applications in the next-generation fibre communication technology [3].

1.1 Rationality of the combination of sol-gel process and optical fibres

In this thesis, the sol-gel process is characterised by the fabrication of silica aerogel or xerogel. A sol is a colloidal suspension of very small solid particles in a continuous liquid medium. The sol-gel process consists of the preparation of a sol, the gelation of the sol and the removal of the solvent [4]. This process requires a relatively low temperature and the products would have a high purity, however the cost of raw materials would be higher than that used in conventional melting techniques.

Silica aerogel is a very light and highly porous form of silica glass, with densities and refractive indices much lower than those of ordinary solids [5]. Such materials, that can be rapidly fabricated, have aroused interest in the enhancement of fibre optics. An aerogel-core waveguide was produced by injecting aerogel into a hollow-core bandgap fibre and it was found that the filling strongly altered the waveguide properties [6]: the filled fibre was able to guide light by total internal reflection (TIR)

over a range of infrared wavelengths and also by photonic bandgaps over a different wavelengths. Coexistence of bandgap- and index-guided modes was also observed.

For a conventional optical fibre, the basic image of a waveguide is that the light is confined inside a core region of solid silica glass, making it inaccessible for other usages such as evanescent field sensing. To release a proportion of the light, fibres could be tapered into a much thinner structure by using a taper rig [7]. Such tapers are very fragile so special protection is necessary. Due to its low refractive index and material compatibility, encapsulation of aerogel around tapered fibres can add a mechanical protection that protects the tapered fibre from contaminants. Moreover, the open nature of the aerogel network allows gas to flow through the material and into the adjacent evanescent field of a tapered fibre [8]. Tapered fibres embedded in bulk aerogel provided over 2 months' protection; the hydrophobic aerogel, as well as being waterproof, also acted as a gas-permeable material [9].

1.2 Novelty of the combination of sol-gel process and optical fibres

Based on the previous exploration of sol-gel techniques and optic fibres, the general idea of the proposed project is the fabrication of aerogel and xerogel to exploit their possible interesting interactions with optical fibres. A new structure of hollow core fibre was designed to investigate intensity-dependent interactions between light and aerogel. It has a much simpler structure than Grogan's hollow core bandgap fibre shown in Fig. 1.1. In this interaction, what we expected is only the total internal reflection (TIR) guidance without bandgap guidance.

A growing number of important applications require the aerogels as thin layers on other substrate materials because most of the properties, such as low refractive index and mechanical protection, which are characteristics of bulk aerogels are also exhibited in thin sheets or films of the material [10]. The fabrication of aerogels in

such fragile forms presents problems due to the weak and tenuous nature of the highly porous structure; special requirements are hence necessary for the formation and drying of aerogels. With similar properties, xerogel films produced through ambient pressure have a slightly higher refractive index than aerogel, but still lower than that of silica glass [11]. Xerogel films are as interesting as aerogel films for the application to optical fibres, such as the low-loss deposition of sol-gel derived silica films on tapered fibres that has been demonstrated with a structural long-period grating with inter-layer variations in refractive index [12].

In this research, attempts were made to fabricate thin aerogel film around tapers as it might protect the fragile tapers as well as control the spacing between two tapers since it strongly affects the evanescent wave coupling efficiency. However, crack-free silica xerogel film was made instead of aerogel film by ambient drying and was investigated for a thorough understanding of its physical and optical properties.

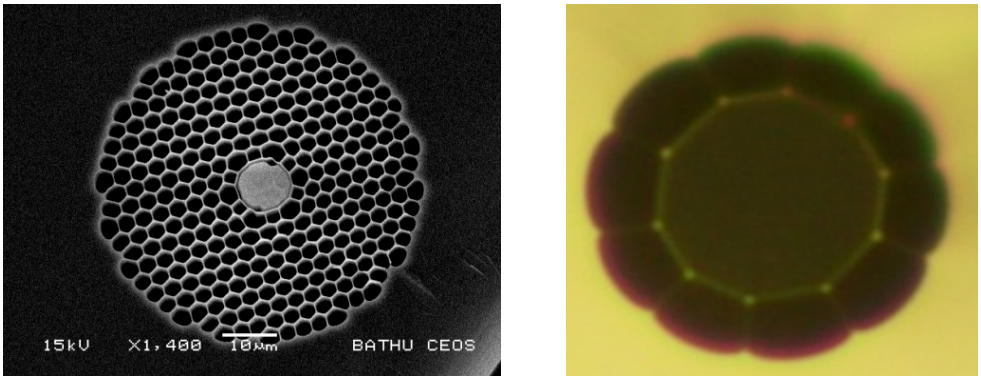

Fig 1.1 Grogan's aerogel core waveguide in HC bandgap fibre (left)[6] and aerogel core waveguide in a TIR designed fibre (selected from section 3.1 in this thesis) (right)

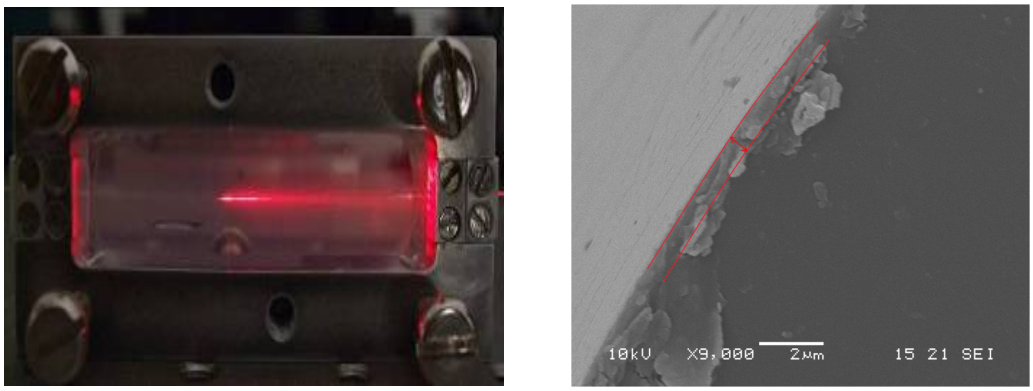

Fig 1.2 Xiao's bulk aerogel proceting around tapers (left) [9]and silica xerogel film around optical fibres(selected from section 5.3 in this thesis) (right)

1.3 Overview

As described in this chapter, the work compiled in this thesis covers the aerogel waveguide in designed optical fibres, silica thin film deposition around fibre and evanescent-wave coupling.

Chapter 2 provides some background knowledge of the sol-gel process and fibre optics, respectively. In the sol-gel process section, descriptions of a substantial field of sol-gel chemistry are presented, along with supercritical drying and a brief introduction to aerogel and xerogel. The optical fibre section, on the other hand, only includes key points of total internal reflection and the properties of tapers and couplers.

Chapter 3 investigates a simple structured hollow core fibre that guides light in aerogel by total internal reflection in a wavelength range over 550nm. An improved filling method was demonstrated that eliminated gaps between aerogel sections suspended in the fibre core; such gaps could be observed using an optical microscope assisted by index matching fluid.

Chapter 4 comprises a collection of deposition methods of thin silica film coating and from them a dip coating method was chosen for the experimentation. A design for the experimental apparatus for coating crack-free thin film is presented followed by the interpretation of control experiments with various coating and aging times in order to optimise the film quality. Thickness and refractive index of the films are characterised.

Chapter 5 presents theoretical analysis on evanescent wave coupling between two tapers, which is then compared with the experimental results. Since the coupling efficiency strongly depends on the spacing of the tapered fibres, initial experimental design for comparing thin film coated tapers with uncoated tapers is illustrated.

A summary of results obtained during the research is presented in Chapter 6. It also includes perspectives of future work related to sol-gel fabrication and applications.

Chapter 2 Background

This chapter contains background information of the sol-gel process and optical fibres. Firstly, the sol-gel process is described and properties of silica aerogel and xerogel combined with explanations of the reason for cracks causation and useful methods of surface modification are introduced. The following section concerns fibre optics: the basic concepts of conventional fibres when light is guided by total internal reflection (TIR) are introduced. Then the fabrication process and potential applications of tapered fibres are also presented in this section as the background knowledge to a better understanding of the work that will be presented in Chapter 4.

2.1 Sol-gel process

In 1931, S. S. Kistler first reported successful removal of liquid from a "jelly" body without collapsing the solid network, and then a new material, aerogel, had been produced from sol-gel processing [13].

2.1.1 From sol to gel

Sol is a type of suspension of liquid and gel. It is a dual phase material of a solid skeleton filled with a solvent. As is shown in Fig 2. 1, sol-gel process starts at a solution (A), after chemical mix it becomes a sol (B), from a sol it can produce thin film by dip, spin or spray coating with the viscosity of a sol adjusted within a proper range. After gelation, the liquid sol can covert to a solid gel (C). Fibres can be made from two ways, drawing from the sol or extrusion from the gel. When the solvent is removed, the wet gel convert to an aerogel (D) through supercritical drying or c a xerogel (E) through ambient drying. Monolithic glass (F) could be effectively produced by cast sintering a xerogel [4].

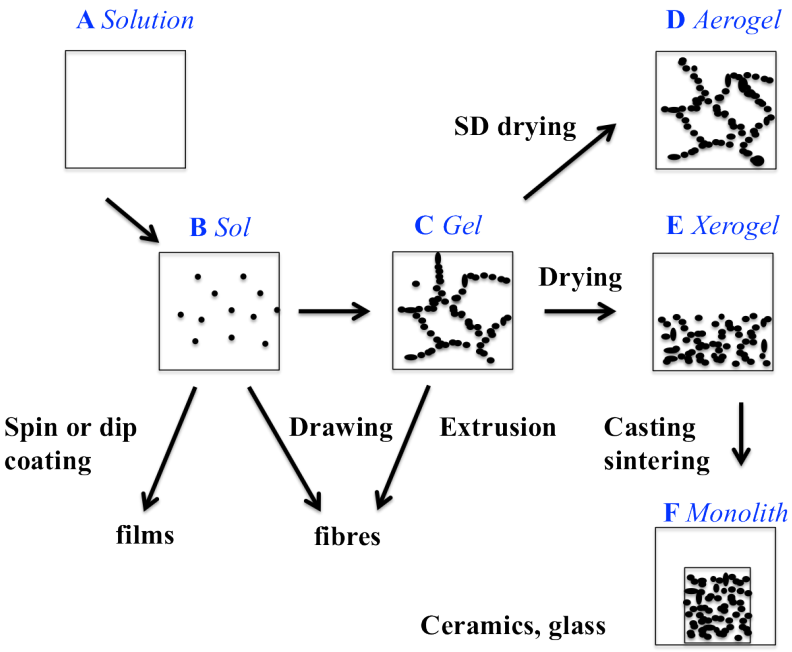

Fig 2. 1 Schematic diagram of sol-gel process

In the sol preparation, the organic or inorganic precursors undergo two chemical reactions: hydrolysis and condensation, typically with acid or base as catalysts to form small solid particles or clusters in an either organic or aqueous liquid solvent. The reactions are describe as[4]:

Hydrolysis: $Si(OR)_4 + 4H_2O \rightleftharpoons Si(OH)_4 + 4ROH$ (2-1)

Water Condensation: $\equiv Si - OH + OH - Si \equiv \rightleftharpoons \equiv Si - O - Si \equiv + H_2O$ (2-2)

Alcohol Condensation: $\equiv Si - OR + OH - Si \equiv \rightleftharpoons \equiv Si - O - Si \equiv + ROH$ (2-3)

In this thesis, all the experiments related to sol-gel process have used tetramethoxysilane (TMOS) as a silica precursor and base catalyst. Presented here is the stoichiometric reaction of TMOS and water:

$$Si(OCH_3)_4 + 2H_2O \rightarrow SiO_2 + 4CH_3OH \quad (2\text{-}4)$$

Once the polymer chains have gelled, the structure is referred to as a wet gel, which corresponds to gel filled with a pure liquid or mixture of liquids. After a wet gel has formed, the next important stage of sol-gel process is aging. Different aging times from zero to several months have been found to produce varying properties.

During the aging process, it is common to do a further exchange or multiple exchanges to replace the intended excessive water in the wet gel, inasmuch as to completely utilise Si molecules from the precursor. The structure of the wet gel alters the continuing reaction of silica precursor and thus the network is stronger due to the primary particles and aggregates adding the edges of the former structure. Meanwhile, un-reacted chemicals undergoing hydrolysis and condensation can enhance the network. Then after sufficient aging time, the structure of the wet gel evolves into a more uniform network [4,14].

The structure can continue its evolution when being dried, but it is dependent on the type of process. There are three ways for the liquid phase to convert to gas phase: freeze-drying, ambient drying and supercritical drying, as illustrated in in Fig 2.2.

Freeze-drying (blue arrow in Fig 2.2) is a process that replaces the solvent with a liquid that can be removed by freezing and subliming to achieve the porous aerogel. However, any water left inside the porous structure will expand when frozen.

Supercritical drying (SCD) marked as red arrow in Fig 2.2 is a method of transforming liquid to gas without the coexistence of two phases. Therefore it allows the structure of the gel to be preserved with the pores to be filled with gas instead of liquid. The transformation happens as the liquid is heated above its critical temperature, while always being held under an instantaneous pressure greater than the vapour pressure as the temperature rises.

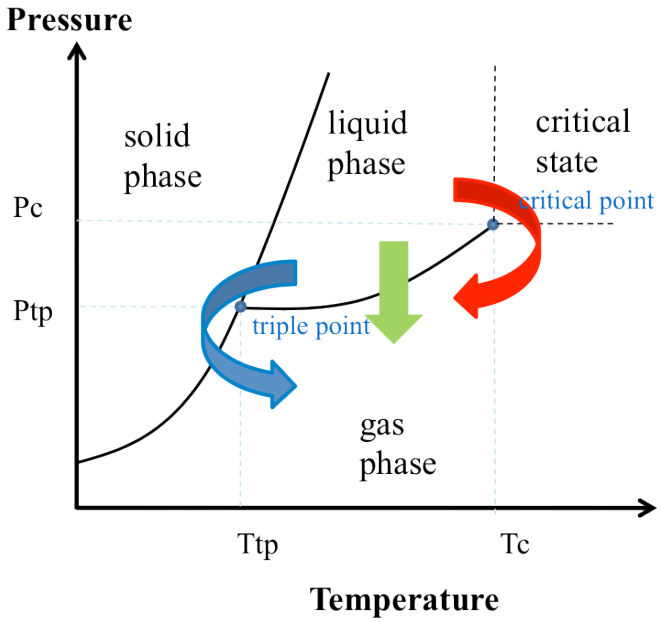

Fig 2.2 Phase diagram showing freeze drying (blue), ambient drying (green) and Supercritical drying (red)

If the evaporation rate from wet gel is sufficiently low, then ambient (evaporative) drying (green arrow) can produce a large shrinkage but an intact dense glass, known as "xerogel". Xerogel is also made of silica, having a refractive index higher than that of aerogel, but still lower than that of glass. But wet gel may crack if the evaporation rate is too high: this is because as more liquid is evaporated and the meniscus recedes into the pore, the larger capillary force from this meniscus destroys the fragile structures [15], as seen in Fig 2.3.

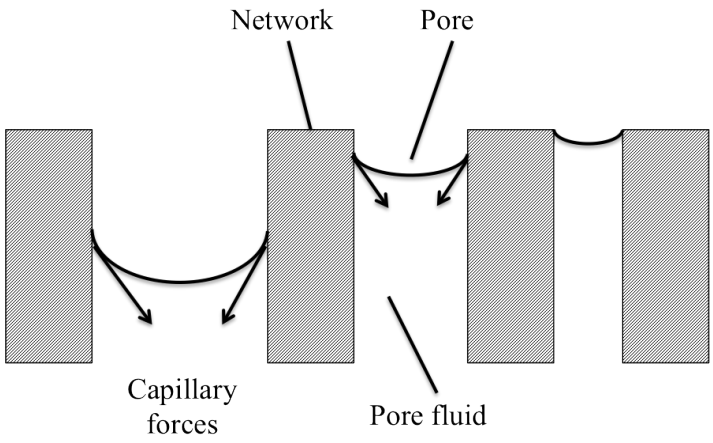

Fig 2.3 Contracting surface forces in pores of different size during drying

The capillary pressure is given in [16]:

$$P = \frac{-2\gamma cos\theta_c}{\gamma_p} \tag{2-5}$$

where P is the pressure, γ_p is the pore radius, γ is the surface tension of the liquid in the pore and θ_c is the contact angle between the liquid and the pore. We have known from experiments with aerogel that the solid component of the network is actually quite strong even at macroscopic scale and the network itself is expected to be much stronger. This is the reason why slow evaporation causes shrinkage: the gel becomes compressed under enormous applied force, but the network resists cracking. However, as the parts of the network approach each other, condensation reactions that expel water produce irreversible bonds so the shrinkage is also irreversible [15].

2.1. 2 Properties of aerogels and xerogel

Aerogel, known as "solid air", consists of chains of bead-like particles with pores in between and has an extremely low refractive index (slightly larger than air). As shown in Fig 2.4 (a), the average size of particles is about 2-5nm, and the diameter of the hole is just under 100nm, which enables aerogel to have a low density ranging from 0.003g/cm^3 to 0.35g/cm^3 [17]. Due to the open network structure, aerogels are good thermal insulators because both gases and silica are poor heat conductors, as can be seen in Fig 2.4 (b). These extraordinary properties arouse interest in many areas and one of the most remarkable applications was to trap space dust particles [18]. The aerogel appears blue in colour due to Rayleigh scattering of visible light that is proportional to λ^{-4}[19].

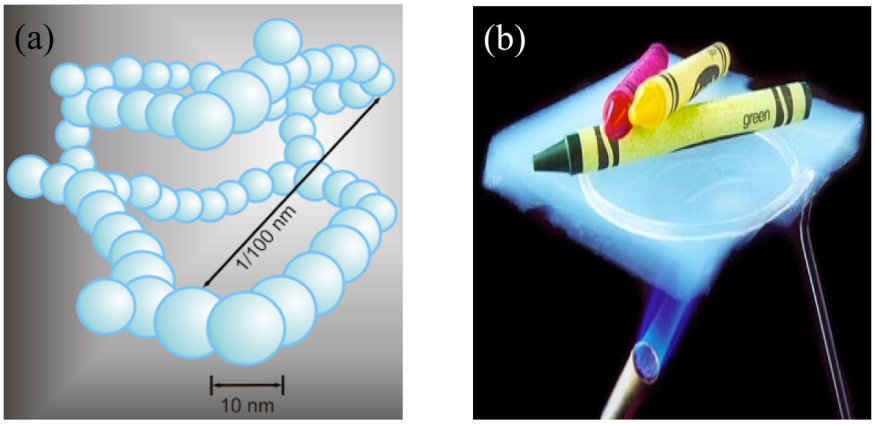

Fig 2.4 (a) Schematic structure of aerogel [4]. (b) Wax crayons on a layer of aerogel protected by its insulating properties from blowing torch fame [5].

Xerogels, although denser than aerogel, still retain a high porosity (15~50%) along with very small pore size (1~10nm) [20]. Heat treatment of a xerogel at an elevated temperature produces viscous sintering (shrinkage of the xerogel due to a small amount of viscous flow) and effectively transforms the porous gel into a dense glass [4]. In such case, nanoparticles or quantum dots can be mixed in different concentrations in the sol and then well dispersed in xerogel or monolith through this process [21].

So far, we know that the main difference between aerogels and xerogels is refractive index. In optics, refractive index describes how light propagates through that medium, which is defined as [22]

$$n = \frac{c}{v} \tag{2-6}$$

where c is the speed of light in vacuum and v is the speed of light in the substance. Aerogel has a refractive index that is dependent on its density. Its refractive index is about 1.01[23], so special methods are required to measure its value [24].

2.1.3 Surface modifications

Both aerogels and xerogels tend to be hygroscopic, that is, they can absorb moisture from the atmosphere and the structure will be destroyed. This is because the surfaces

are covered in hydroxyl groups that present sites for hydrogen bonding [25]. These sites attract water that condenses on the internal surfaces. Liquid water drops are destructive because the large quantity of surface OH within the aerogel will pull the drop into the bulk, and the structure will shatter into white powder due to capillary forces as previously described in 2.1.1.

Improved hydrophobic properties can be obtained by linking CH_3 directly to Si in the network. Methyltrimethoxysilane ($CH_3Si(OCH_3)_3, MTMS$) co-precursor provides three network bonding sites, and presents on external hydrophobic termination [26], as illustrated in Fig 2. 5 (a). Alternatively, the aerogel can also be made hydrophobic by washing the wet gel with hexamethyldisilazane ($(CH_3)_3SiNHSi(CH_3)_3, HMDS$) during aging (Fig 2. 5 (b)). If the network is already stable, the surface can be modified with little effect on the optical properties. Trimethylsilyl (TMS) modification of the surfaces is more effective by adding three hydrophobic groups per surface site on a branched structure [27].

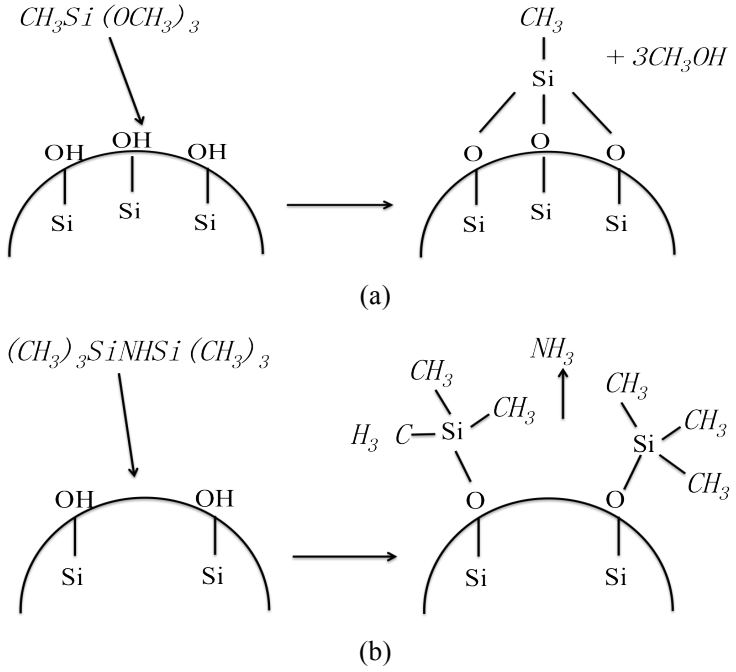

Fig 2. 5 Different methods of producing hydrophobic aerogel (a) using a co-precursor (MTMS) to coat the internal surfaces with a single hydrophobic (CH_3) group in place of the hydroxyl group. (b) Surface modification by washing with HMDS after the wet gel has already formed.

Until now, we have reviewed the sol-gel chemistry and the properties of both aerogel and xerogel. The next section will discuss fibre optics, which is another import fundamental material towards the topic of sol-gel and fibre optics.

2.2 Fibre optics theory

In the early 1840s, the possibility of guiding light through jets of water was first demonstrated. This was the foundation for optical fibres that transformed today's global communication networks [28]. In this section, fundamental theory of optical fibres will be discussed.

2.2.1 Conventional fibres

The structure of a conventional optical fibre is shown in Fig 2.6. It consists of a core, a cladding and a coating (buffer and jacket). The glass core has a diameter from a few microns to a few tens of microns surrounded by a typically 125μm glass optical cladding. The coating is plastic, protecting the fibre from contamination and damage.

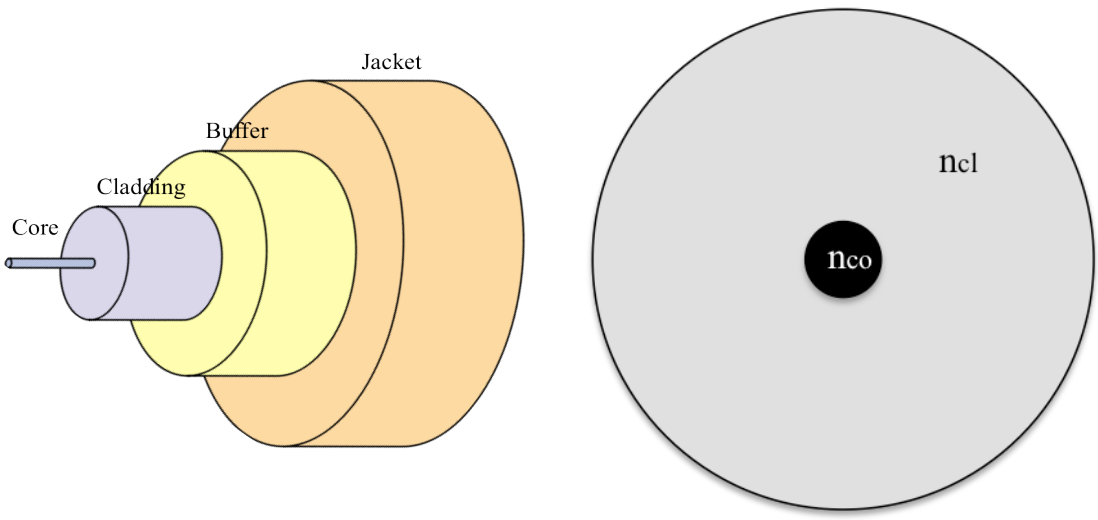

Fig 2.6 The structure of a conventional fibre, n_{co} is refractive index of core and n_{cl} is the refractive index of cladding.

Generally, the core is filled with dopants, such as germanium to ensure that the light

is guided through total internal reflection (TIR). According to Snell's law, light incident on a boundary between two different materials of differing refractive index,

$$n_1 sin\theta_1 = n_2 sin\theta_2 \tag{2-7}$$

where θ_1 and θ_2 are the angle of incidence and angle of refraction respectively, and n_1 and n_2 are the refractive indices of the materials, providing $n_1 > n_2$, the critical angle is given by:

$$\theta_c = arcsin\,(\frac{n_2}{n_1}) \tag{2-8}$$

As for the case in optical fibres, which is shown in Fig 2.7, the boundaries are identical low index materials surround a high index core ($n_{core} > n_{cladding}$). The light that is totally reflected at the first boundary will also be totally reflected at the second as well. When $\theta_1 < \theta_c$, the light is both reflected and refracted. When $\theta_1 > \theta_c$, all of the light is reflected, at which time we say that light is confined by TIR [29].

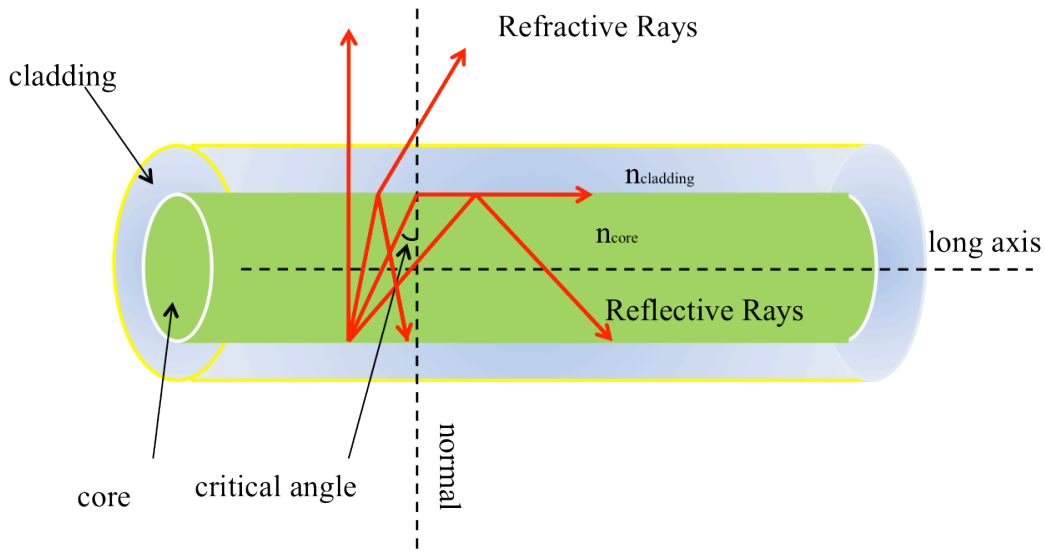

Fig 2.7 Schematic of light transmission through a conventional optical fibre

Optical fibres can be categorised into single- and multi-mode. Modes are the mathematical solution of Maxwell's equations and physically imply the distribution of the electromagnetic fields. The propagation constant β represents the change in phase as it varies with distance. The permitted values of β in a TIR-guiding fibre are limited by the refractive indices of the core and cladding regions and are given by [29]

$$n_{cl}k_0 \leq \beta \leq n_{co}k_0 \tag{2-9}$$

where n_{cl} and n_{co} are the refractive indices of the cladding and core respectively, and $k_0 = {}^{2\pi}/_{\lambda}$ is the free-space wavenumber. As light exits optical fibre at an angle that depends on β, it is useful to define an effective refractive index, n_{eff}, of a particular mode with a propagation constant β as

$$n_{eff} = \frac{\beta}{k_0} \tag{2-10}$$

so that this relation becomes $n_{cl} \leq n_{eff} \leq n_{co}$.

For TIR guidance, light needs to be launched into an optical fibre so that it propagates with an angle less than the critical angle, θ_c. We can define a numerical aperture (NA) as shown in Fig 2.8

$$(\mathrm{NA}) = \sin(\theta_{max}) = \sqrt{n_{co}^2 - n_{cl}^2} \tag{2-11}$$

Thus light fills a cone with a half angle given from $\sin^{-1}$(NA).

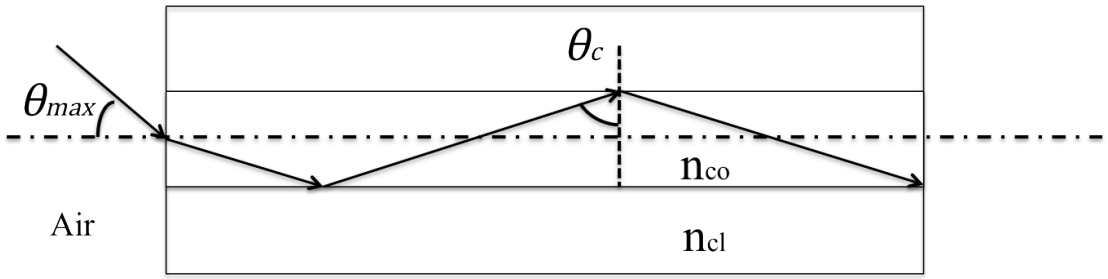

Fig 2.8 Profile view of a TIR guidance optical waveguide.

Normalized frequency, known as the V value, determines the number of modes supported in the core for a particular wavelength of light. The equations is described as [29]

$$V = \frac{2\pi}{\lambda}\rho\sqrt{n_{co}^2 - n_{cl}^2} \tag{2-12}$$

where ρ is the core radius and λ is the wavelength of light. Conventional optical fibres will only support the fundamental mode and no higher order modes if the condition $V < 2.405$ is satisfied [29,30].

2.2.2 Tapered fibres

Tapered fibres or tapers are fibres with a varied radial dimension. The taper rig in the Centre for Photonics and Photonic Materials (CPPM) at University of Bath can form taper transitions and waists of many shape and size by precise control of taper parameters. Low loss tapers have been demonstrated that changes the radial dimensions of the fibre from $125\mu m$ down to just a few hundred nanometres [31].

The process is controlled by a computer program that drives the two translation stages: the burner and elongation stages marked in Fig 2. 9. The butane-oxygen flame sweeps quickly back and forth along the fibre, simultaneously the fibre is stretched from both ends. Since the hot zone is small (~1mm), only a part of the fibre that instantaneously contacts the flame is stretched.

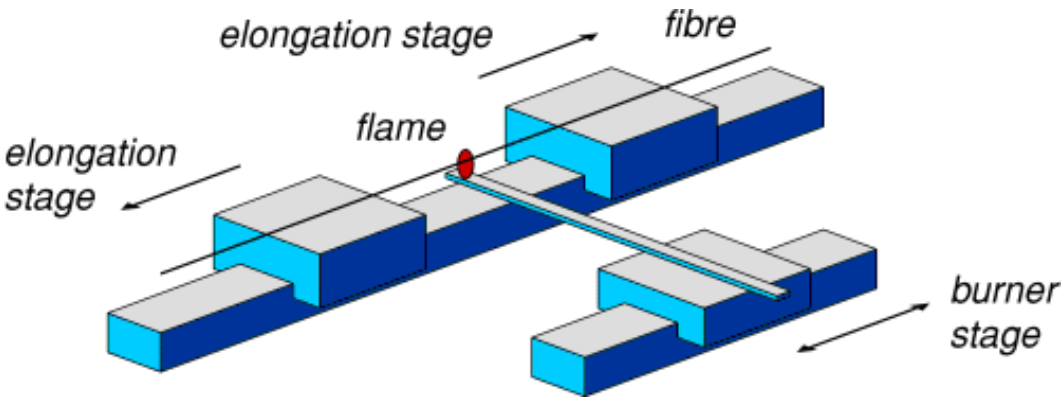

(a)

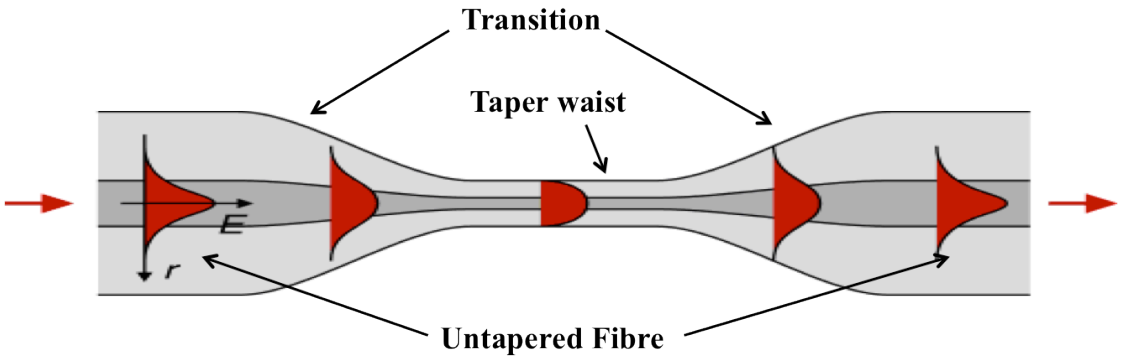

(b)

Fig 2. 9 Schematics showing (a) the tapering rig and (b) the shape of a taper and mode transmit through a taper[31].

The modes of light propagation in a taper waist can be very different from that in the input fibre. However, if the taper transition is gradual enough, light in the fundamental mode of the input fibre will be coupled entirely to the light in the fundamental mode of the taper waist. These gradual transitions are necessary to make adiabatic tapers from single-mode fibre lossless which is the adiabaticity criteria given by J. D. Love et al. Confinement of optical energy in one mode can be achieved by an adiabatic taper transition, where the energy transfer between different modes is negligible [32].

As shown in Fig 2.5, in order to acquire lossless tapers, the taper transition has to vary gradually: the local taper length-scale L_t, is larger than the coupling length scale L_b between the relevant modes, which can be expressed as [32]

$$L_t(z) > L_b(z) \tag{2-13}$$

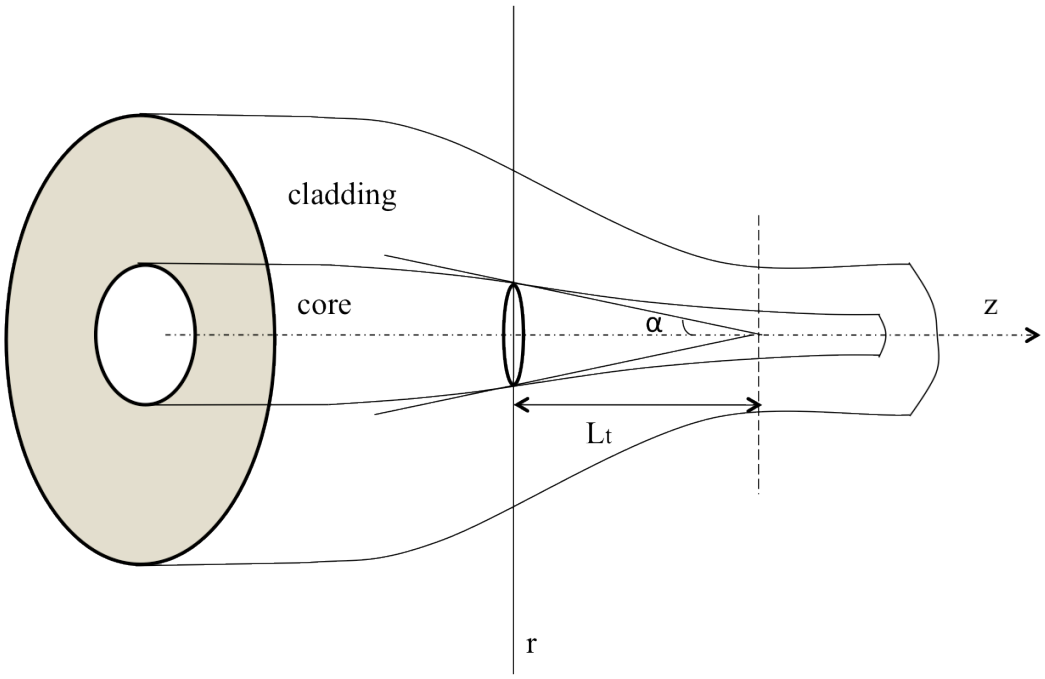

Fig 2.5 Tapered single-mode fibre showing finite cladding

The local taper length-scale L_t defined as the height of a right circular cone with base coincident with the local core cross-section and apex angle equal to the local taper angle. The local coupling length-scale of two modes, L_b, is taken to be the beat length of these two modes:

$$L_t(z) \approx \frac{r(z)}{\alpha} \tag{2-14}$$

$$L_b(z) = \frac{2\pi}{\beta_1(z) - \beta_2(z)} \tag{2-15}$$

where z is the axial coordinate, $\beta_{1,2}$ are the propagation constants of the fundamental mode and the most adjacent high-order mode in the transition part, respectively, r is the fibre radius, and $tan\alpha = \left|\frac{dr(z)}{dz}\right|$ is the decreasing slope of the fibre radius along the axis.

If $L_t(z) \gg L_b(z)$ all over the taper, then coupling will be negligible and the fundamental mode will propagate approximately adiabatically with negligible loss. Conversely, if $L_t(z) \ll L_b(z)$ there will be significant coupling to the other mode. Accordingly, the condition $L_t(z) = L_b(z)$ provides an approximate delineation between approximately adiabatic and lossy tapers [32].

For a conventional fibre, the evanescent field only occurs in the cladding, but in the taper it often comes out of the fibre which means there is more optical energy around the fibre and light will propagate in the air instead the core when in a tapered fibre waist, which provides numerous areas of interests such as directional coupler. As shown in Fig 2.6, two parallel guides are placed sufficiently close together so that these parts of the evanescent field will overlap spatially therefore light can be coupled from one waveguide to the other [30].

For power input in fibre 1 (as shown in Fig 2.6), the power output varies sinusoidally as:

$$P_2(z) = P_0 F^2 sin^2(\frac{C}{F} z) \tag{2-16}$$

$$P_1(z) = P_0 - P_2(z) \tag{2-17}$$

Where C is the coupling coefficient, which is a function of wavelength, core separation, size and refractive index. P_2 stands for the coupled power and P_1 represents the transmitted power.

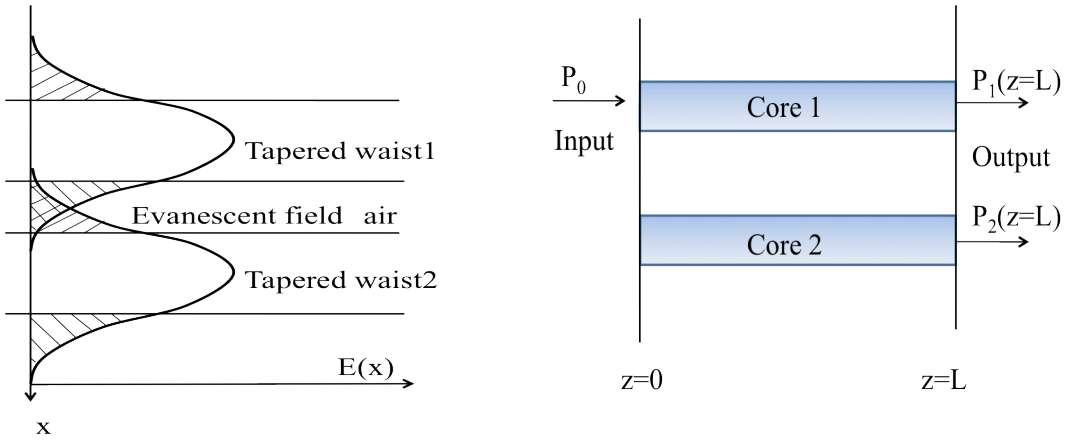

Fig 2.6 (Left): Schematic showing the overlap of the evanescent fields of two tapered fibre in their waists. (Right): Conceptual representation of the coupling process. When power is launched into one core, the power will couple into the second core.

The behaviour of a directional coupler depends on the dissimilarity of the cores, which is indicated by the F^2 factor.

$$F^2 = \frac{1}{(1 + \frac{(\beta_1 - \beta_2)^2}{4C^2})} \tag{2-18}$$

where β_1 and β_2 are the propagation constants of the fundamental modes present in the isolated first and second cores respectively. In a symmetric coupler the two cores are identical and when considered separately their fundamental modes will have the same propagation constants $\beta_1 = \beta_2$ so that $F^2 = 1$. This happens for any value of C. In this case, complete power transfer between the two cores can be reached. Otherwise if the coupler is asymmetric $\beta_1 \neq \beta_2$ so that $F^2 < 1$.However when C is large compared to the difference of propagation constants $2C \gg |\beta_1 - \beta_2|$, then $F^2 \approx 1$ and nearly complete power transfer will occur. Otherwise, if $2C \ll |\beta_1 - \beta_2|$ and $F^2 \approx 0$, which is a negligible transfer of power, an extreme case occurs that is

called the null coupler [33].

2.3 Conclusions

This chapter provides the background required for the subsequent chapters involving sol-gel process and fibre optics. The detailed sol-gel chemistry accompanied with the properties of aerogel and xerogel was reviewed as a significant understanding of sol-gel derived thin film (Chapter 4). Meanwhile, TIR of conventional fibre, the operations of taper rig with aerogel core and couplers have been discussed for the work of fibre with aerogel core (Chapter 3) and evanescent-wave coupling(Chapter 5). It is through the understanding of these topics that progress has been made towards the goal of combing sol-gel process and fibre optics.

Chapter 3 Fibre with aerogel core

3.1 Introduction

As we have already discussed the background of fibre optics and sol-gel process, in this chapter we will discuss one of the combinations of these two subjects, namely fibre with aerogel core.

In chapter 2, the guidance of conventional fibres is presented as a result of TIR and the core is usually doped with materials that have a refractive index larger than that of the cladding. We know that aerogel has a low refractive index, which is slightly larger than air, however, if the microstructure of a fibre is particular designed, aerogel can also act as a waveguide that guides light though TIR in certain wavelength range. This is very interesting as aerogel can hold nanoparticles well dispersed, which will enhance the optical functionality to fibres; on the other hand, packing aerogel with fibres will protect aerogel from damage due to its fragility.

In 2010, M. Grogan selectively filled aerogel into the core of a hollow core bandgap fibre [6]and it was found that the light was guided by different mechanisms varying with wavelength: a photonic bandgap guided light of short wavelengths, while aerogel core guided light by total internal reflection at long wavelengths, and there is an overlap of both bandgap- and index-guided region [6]. Since infrared transmission is widely used in laser surgery, these results inspired the design of a simple microstructure fibre with only one layer of cladding. It will only guide light by one mechanism, which is total internal reflection in long wavelengths and will enhance the guidance in infrared region.

3.2 TIR fibre design

In order to obtain aerogel core guided by total internal reflection, the cladding requires special design to have a cladding effective index that is lower than aerogel. Fig 3.1 demonstrates the schematic of the cross section of designed TIR fibre and a photo of cross section of fabricated TIR fibre.

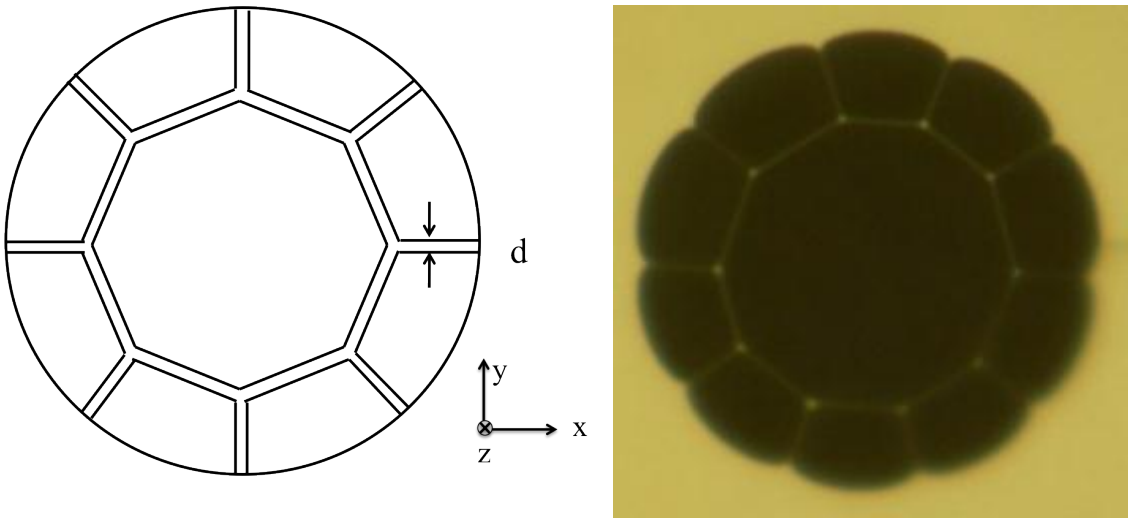

Fig 3.1 A schematic graph (left) and a photo (right) of designed fibre for aerogel filling. $r_{core} = 7\mu m$, $r_{cladding} = 2\mu m$, $d = 54nm$.

As the cladding interval distance d is much smaller compared to the length of the boundaries, the effective refractive index could be estimated by calculating that of a symmetric slab waveguide.

In a symmetric slab waveguide as illustrated in Fig 3.2,

$$n(x) = \begin{cases} n_1, & |y| < a \\ n_2, & otherwise \end{cases}$$

where $a = \frac{d}{2}$. As in the case of aerogel fibre, $n_1 = n_{silica} \approx 1.45$, $n_2 = n_{air} = 1$, and $a = 27nm$.

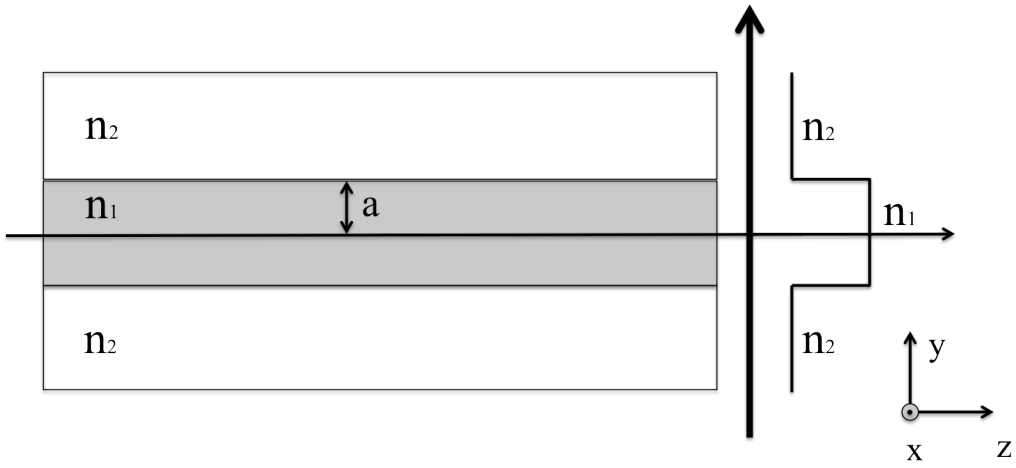

Fig 3.2 A schematic of a slab waveguide

The propagation equation is given as [35]

$$W = -UcotU \tag{3-1}$$

$$W = UtanU \tag{3-2}$$

where the intermediate parameters $U = \sqrt{(k_0^2 n_1^2 - \beta^2)}a$, $W = \sqrt{(\beta^2 - k_0^2 n_2^2)}a$, and $U^2 + W^2 = a^2 k_0^2 (n_1^2 - n_2^2) = V^2$. A graphic solution is shown in Fig 3.3. Since U and W must be positive, the propagation constant β may be found in this case from the intersection of the curve (black dots). It was noticed that the number of solutions depends on the value of V. For the fundamental mode which has the largest β, we can see in the graphic solution, it has the smallest U.

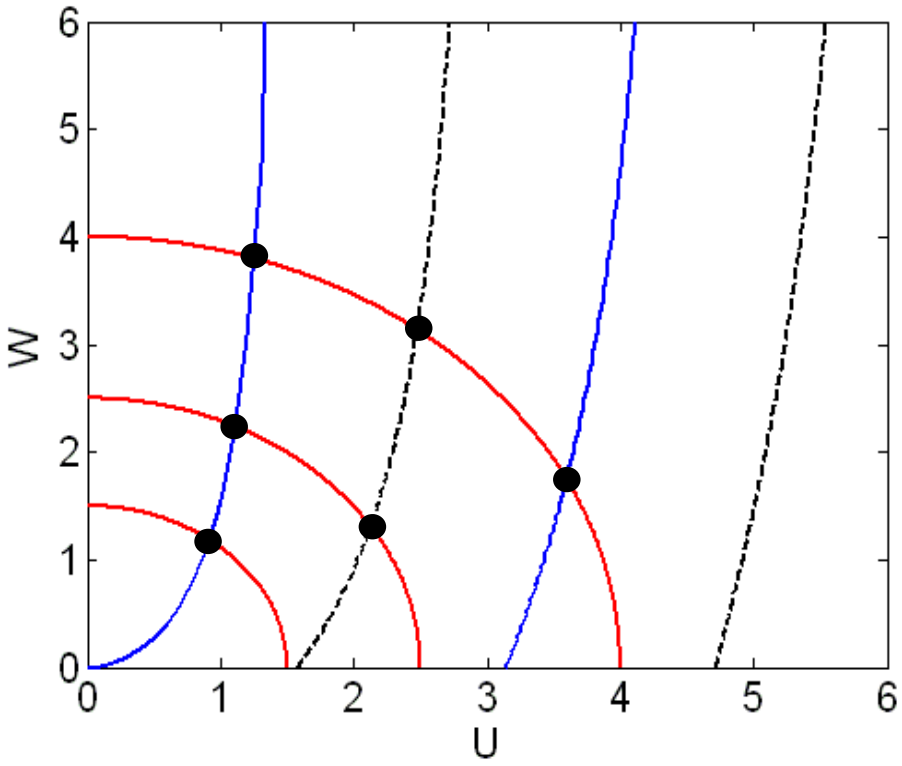

Fig 3.3 Graphic solution of Eqs. (3-1) and (3-2) for three values of V; solid blue curves are $W = UtanU$, and the dashed curves are $W = -UcotU$.

From the graph and the equation (3-1) and (3-2) can be presented the discussion of the range of effective refractive index $\frac{\beta}{k_0}$:

(1) When $V \to \infty$, then $U \to \frac{\pi}{2}$, as $U = \sqrt{(k_0^2 n_1^2 - \beta^2)}a$, so $\frac{\pi}{2} = a\sqrt{(k_0^2 n_1^2 - \beta^2)}$, thus we have $\beta^2 = k_0^2 n_1^2 - \frac{\pi^2}{4a^2}$, if $k_0^2 n_1^2 \gg \frac{\pi^2}{4a^2}$, so $\beta^2 \approx k_0^2 n_1^2$, then $\frac{\beta}{k_0} \approx n_1$.

(2) When $V \to 0$, then $U \approx V$, so we have $a\sqrt{(k_0^2 n_1^2 - \beta^2)} \approx a\sqrt{k_0^2(n_1^2 - n_2^2)}$, then $\frac{\beta}{k_0} \approx n_2$

We know that $V^2 = a^2 k_0^2 (n_1^2 - n_2^2)$, where $k_0 = \frac{2\pi}{\lambda}$, thus V is a monotonically decreasing function of λ, so we have $\lambda \to 0, \frac{\beta}{k_0} \to n_1$, and $\lambda \to \infty, \frac{\beta}{k_0} \to n_2$.

From Equation (3-2), we have

$$\sqrt{\frac{\left(\frac{\beta}{k_0}\right)^2 - n_2^2}{n_1^2 - \left(\frac{\beta}{k_0}\right)^2}} = tan\left(\sqrt{n_1^2 - \left(\frac{\beta}{k_0}\right)^2} \cdot k_0 \cdot a\right) \tag{3-3}$$

Thus $k_0 \cdot a = \frac{arctan\sqrt{\frac{\left(\frac{\beta}{k_0}\right)^2 - n_2^2}{n_1^2 - \left(\frac{\beta}{k_0}\right)^2}}}{\sqrt{n_1^2 - \left(\frac{\beta}{k_0}\right)^2}}$ since the right hand side of the equation that contains k_0 are as the expression of $\frac{\beta}{k_0}$. We only put $k_0 = \frac{2\pi}{\lambda}$ in the left side of the equation, thus the mathematic relationship between λ and $\frac{\beta}{k_0}$ is given by:

$$\lambda = \frac{2\pi a\sqrt{n_1^2 - \left(\frac{\beta}{k_0}\right)^2}}{arctan\sqrt{\frac{\left(\frac{\beta}{k_0}\right)^2 - n_2^2}{n_1^2 - \left(\frac{\beta}{k_0}\right)^2}}} \tag{3-4}$$

where $n_2 < \frac{\beta}{k_0} < n_1$.

From equation (3-4), given the range of $1 < \frac{\beta}{k_0} < 1.45$, we can plot the relationship between λ and $\frac{\beta}{k_0}$ for with $a = 27nm$ fibre used in these experiments. In order to obtain the variation of $\frac{\beta}{k_0}$ with λ, we turned over the graph that plotted from Equation (3-4) to get Fig 3.4.By adding a line that represents $n = 1.045$, which is the refractive index of aerogel that governed the wavelengths where light can be guided in an aerogel core by TIR, the corresponding λ_0 was calculated to be $584.7nm$. In the case of $\lambda > \lambda_0$, light can be guided by TIR whereas when $\lambda < \lambda_0$ light cannot be guided. We therefore expect to see the aerogel-guided light by TIR in the experiment

at wavelengths that are longer than 584.7nm.

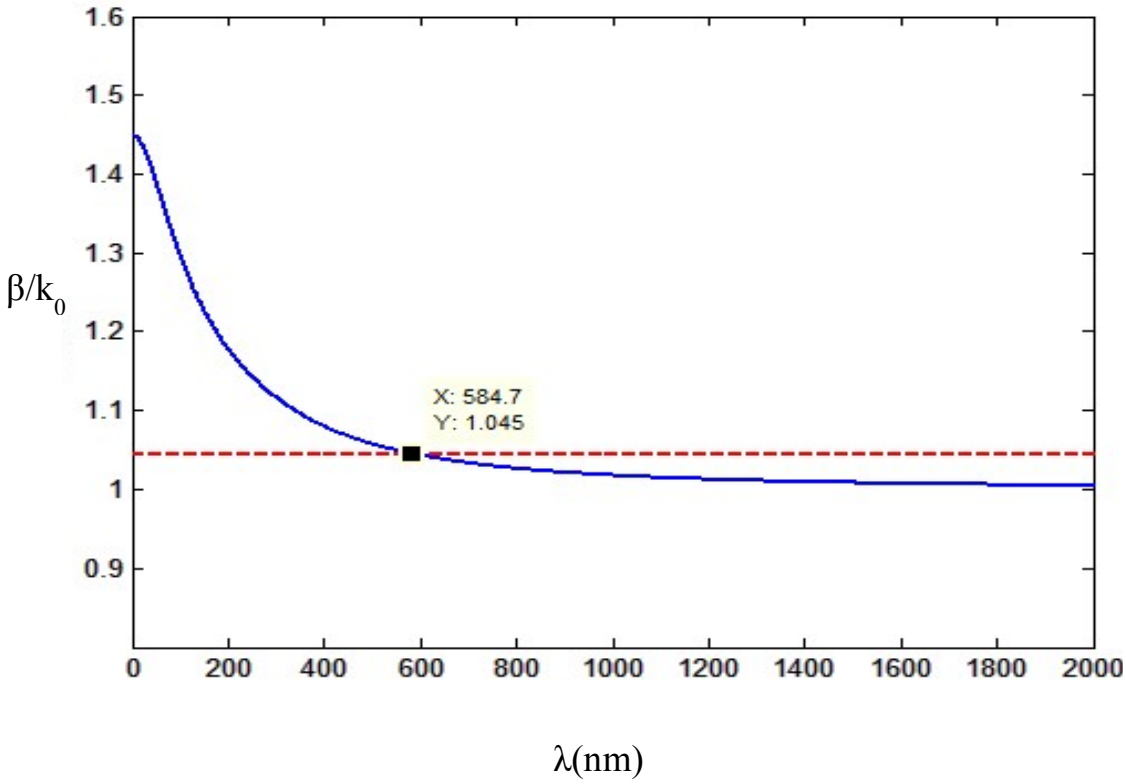

Fig 3.4 Assume that $n_1 = n_{silica} \approx 1.45$, $n_2 = n_{air} = 1$, the thickness of the slab waveguide is 27nm. The blue line is the refractive index of the cladding while the red dashed line is the refractive index of aerogel $n_{aerogel} = 1.045$[14], so the crossing point is 584.7nm.

3.3 Experimental procedure

The filling process of fibre with aerogel could be divided into two steps: filling the fibre with sol and supercritical drying. The former step required controllable gelling time to ensure the quality of filling length and aging processes; while in the later one the wet gel filled fibres were dried in a test tube using supercritical drying rig.

3.3.1 Filling TIR fibre with sol

A schematic of the equipment used to fill fibre with sol is shown in Fig 3.5. The inlet

of the fibre was dipped in the test tube containing the sol, while the other end was attached to a vacuum pump. Fixing one end of the fibre to a vacuum pump created a driving pressure that drew the liquid into the fibre.

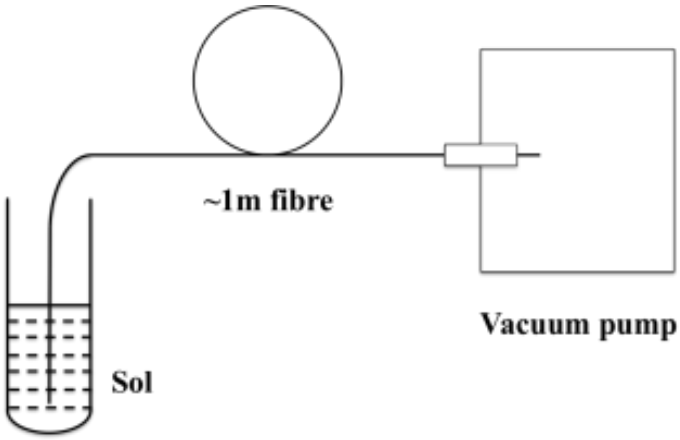

Fig 3.5 A schematic of the vacuum pump equipment used for filling fibre with sol.

The sol was a mixture of TMOS, MTMS, Methanol, water and ammonia. The reaction between TMOS and water was given in Chapter 2, here the methanol was used as the co-solvent: since TMOS and water are miscible, methanol could help the solvents mix into the same phase and react with each other. Ammonia was used as a base catalyst to speed the reaction while MTMS modified the surface hydrophobicity. The molar ratio was given in Table 3-1 and the gel time was about 40 min. The fibre was immersed in methanol containers for the duration of the gelation for one week and during the aging process, several solvent exchanges were necessary to eliminate the redundant water inside the wel-gel.

Chemicals	TMOS	MTMS	Methanol	Water	Ammonia
Molar ratio	1	0.11	2	4.5	3.3×10^{-3}

Table 3.1 Molar ratios of the components in the sol[14].

3.3.2 Supercritical Drying (SCD)

The purpose of supercritical drying is to produce a non-collapsed nanostructure during the removal the liquid, which is fully described in Section 2.1. The photograph of the rig is shown in Fig 3.6. The wet gel filled fibre in a glass container was placed inside the autoclave (A); the oven (marked B) ensured the air temperature in the oven did not exceed 160℃ throughout the operation and protected the user in case of leakage. At the beginning of the process, the autoclave was pressure tested to 100bar using nitrogen gas (C) and it was checked for gas leakage; also it created an inert atmosphere inside the autoclave before the heating started. The pressure was then reduced to 10bar at the starting point. After that the wetgel-filled fibres in the autoclave were heated by an electrical heater (D) every ten minutes until it reached 280℃ at the end of the process, and the pressure needed to be adjusted by opening the outlet valve to ensure it did not exceed 100bar. The bottle (E) was used to capture the waste methanol. The depressurisation rate was kept as low as possible and a reduction rate of 2bar/min was found in the practice that allowed the production of an intact aerogel[14].

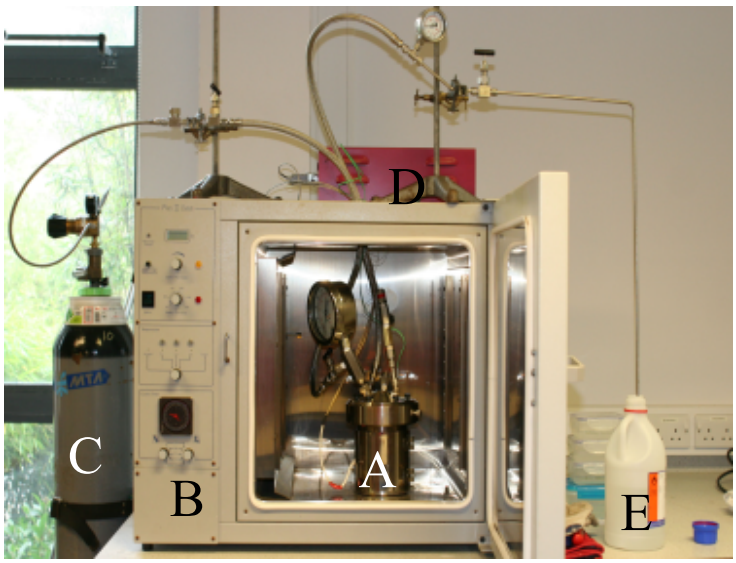

Fig 3.6 A photograph of the high-temperature SCD rig [14]

Before putting fibres into the autoclave, the coating of the fibre was removed to prevent it from burning under a high temperature; the bare fibre was cut into different lengths to monitor the position it had been filled: for example, 8cm of fibre was filled from sol end which grow 1cm at a time up to 16cm from the pump end(Fig 3.7). It was a useful method to identify the optimal part of fillings at the beginning and these pieces were all put into glass test tubes as containers since glass could stand for the high drying temperature of 280℃. As for longer fibres, they were circled around a custom wire net (Fig 3.8)that securely held fibres and allowed easier operation with methanol to drain and evaporate.

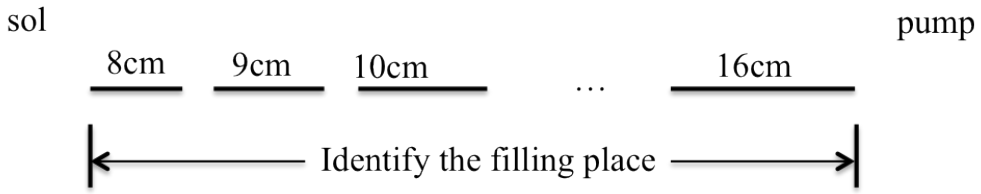

Fig 3.7 Identify the filling place by cutting the fibre into different length

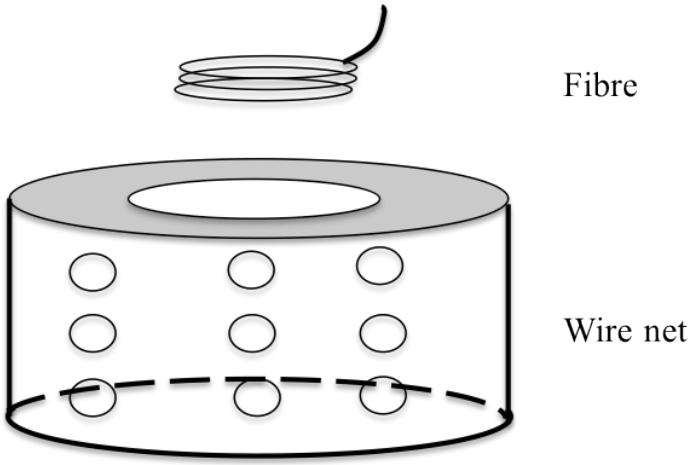

Fig 3.8 A schematic of wire net used for long fibre drying process

The total process took about 1.5 hours to raise the temperature from room temperature to 280℃ and a pressure of 100bar. This was followed by a slow reduction of the temperature over a period of one hour. If all the procedures went well and no leakage happened, then fibres filled with aerogel would be ready for further experimentations.

3.4 Results and discussion

In this section, we will discuss the results that were obtained from the process presented above, combined with problems when dealing with the results and improvements.

3.4.1 Filling area

After supercritical drying, the fibre was cleaved and observed under microscope. A large region of the fibre was found to be filled with aerogel both in the core and cladding and continued until a length of 40cm from the sol side, which was nearly half length of the filled fibre. Fig 3.9 shows images that were taken near the sol end and 30cm from the sol end. We can see that in Fig 3.9(a) aerogel filled nearly all of the cladding, and aerogel in the core shrunk remarkably, while in Fig 3.9(b), there were less cladding filled with aerogel and the aerogel core shrunk a little (less than 25%) .

(a) (b)

Fig3.9 Aerogel in both core and cladding:(a) near the sol end (b) 30cm from the sol end.

Given the size difference between the core and cladding holes in the designed aerogel fibre ($r_{core} = 14\mu m,\ r_{cladding} = 4\mu m$), the length that sol flowed into the cladding cannot be neglected. Therefore, it was necessary to block the cladding with glue to ensure that only the core was filled with sol. The cladding was then blocked in one

end and the blockage at both sol and the pumping ends were tested and both of them could successfully prevented the sol from infiltrating the cladding. Since the results were not significantly different with either schemes, the blocked cladding end was chosen near the pump in the following experiments for the sake of avoiding contaminating the sol.

After blocking the claddings, fibre with fully filled aerogel core was much easier to obtain. Fig 3.10 (a) indicates the cross-section of the original fibre with no gel, Fig 3.10(b) shows the wet-gel filled fibre after blocking the claddings and Fig 3.10(c) illustrates the fully filled aerogel core after supercritical drying process. It can be seen that there was almost no shrinkage from wet gel core to aerogel core; the shrinkage shown in Fig 3.11(a) and (b) was a result of the contact of the wet gel with air during the cutting process that might cause cracking and 25% shrinkage by the capillary force. Practice suggested that cutting about 1.5-3cm of the end of the fibre would achieve a non-shrunk aerogel core as shown in Fig 3.11(c) and (d).

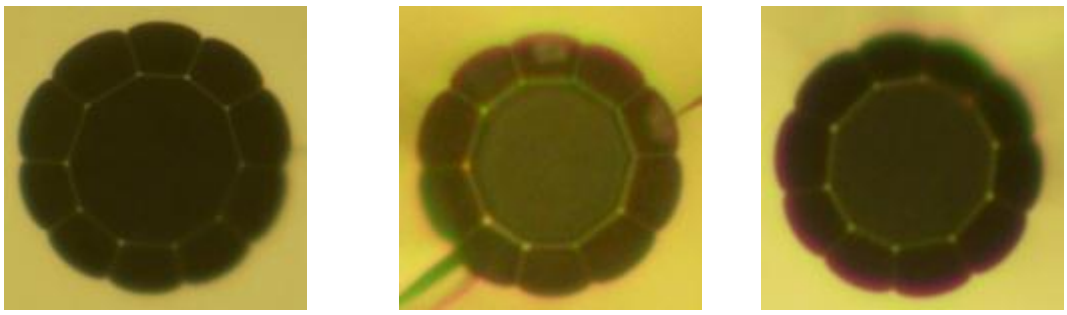

(a) (b) (c)

Fig 3.10 Photographs of different filling cores of aerogel fibres. (a) Fibre with no gel. (b) Fibre with wet gel. (c) Fibre with aerogel

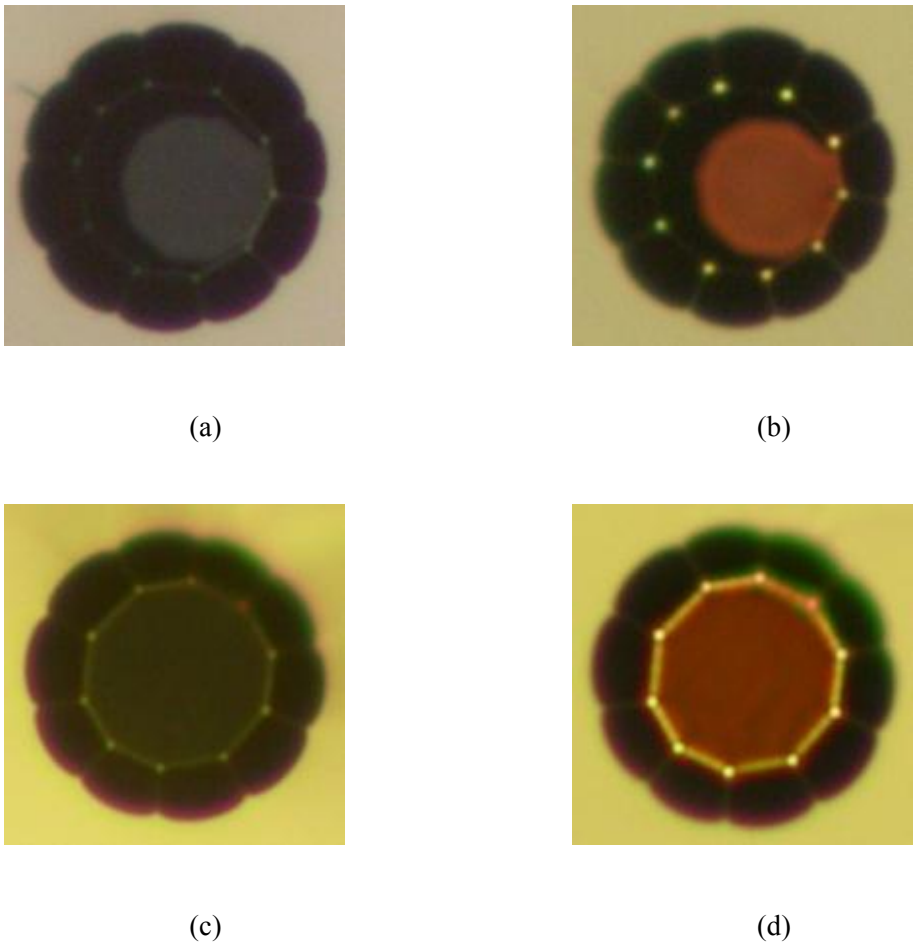

(a) (b)

(c) (d)

Fig 3.11 Images of shrunk aerogel core and fully filled aerogel core under the microscope. (a) Core aerogel shrinkage. (b) Core aerogel shrinkage; illumination was from the other facet of the fibre. (c) Fully filled aerogel core. (d) Fully filled aerogel core under the illumination from the other facet of the fibre. The core with a higher brightness than in (c) might suggest that the waveguiding was successful.

3.4.2 Optical transmission

To ensure the whole length of fibre was filled with aerogel, inspection from both ends of the cross-section of the fibre was required. After cutting off the shrinkage core of the fibre, finally, a 5cm piece of fibre with only core filled was obtained and measured using a Si CCD camera and InGaAs (Indium-Gallium-Arsenide) infrared camera to reveal the way light propagated in the aerogel core. The signal light was emitted by a supercontinuum source, as shown in Fig 3.12. The light passed through

the test fibre and was focused by a 60× lens. The near field pattern of the end of the fibre (red dot) was displayed on the white screen.

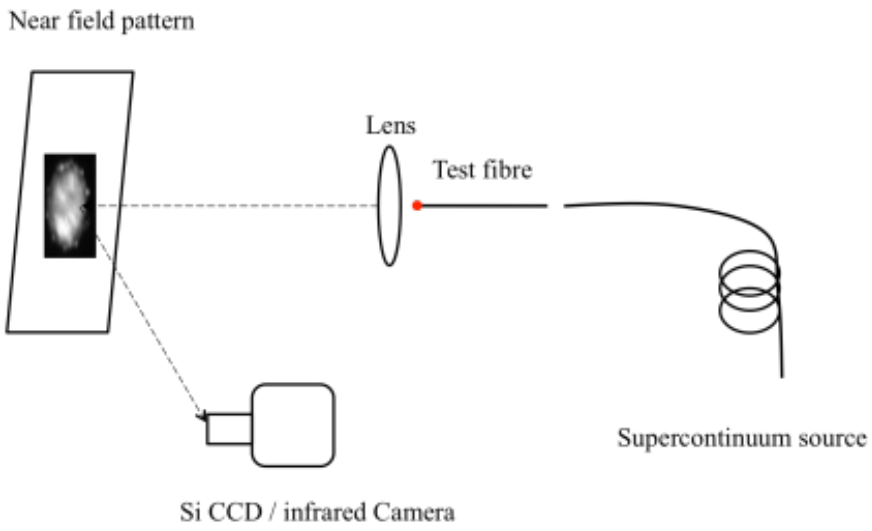

Fig 3.12 Setup of the near field pattern measurement

As was shown in Fig 3.13, the pictures of near-field images from 530 to 850nm were taken by the Si CCD camera with different band pass filters while those wavelengths greater than 1050 were captured by InGaAs (Indium-Gallium-Arisenide) infrared camera. In Fig 3.13, we can see that the light was confined in the core and when the wavelength moved into the infrared region, the light became brighter and the small bright dots at the edge of the core were indistinct compared to that in shorter wavelength. The results obtained in Fig 3.13 were in correspondence with the theoretical analysis in Fig 3.4 for guided wavelength longer than 584.7nm.

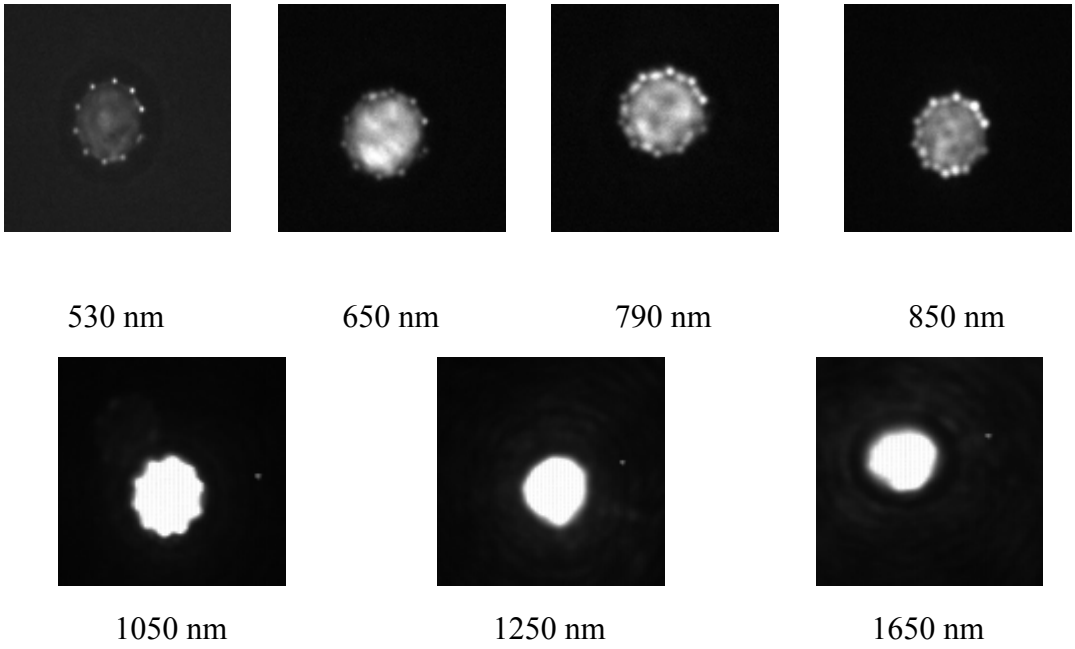

Fig 3.13 The near field pattern of different wavelengths for the designed fibre filled with aerogel only in the core area.

3.4.3 Filling profile examination

In order to understand the attenuation in the fibre filled with aerogel core, we attempted a longer fibre of 20cm, however, there was no light coming out of the end of fibre through near field measurement shown in Fig 3.12, even after both of the ends of test fibre were observed fully filled aerogel core.

By cutting the 20cm fibre into small pieces, filling quality was examined. We found that some images revealed an empty area in the core of the fibre, but when defocusing the microscope, the area that appeared empty, actually contained aerogel (see Fig 3.14). This may be due to the cleaving process which may have separated the aerogel slightly differently on two ends, which would not be level with the cladding and gave the illusion of not filling in the core（see Fig 3.15）. This phenomenon impeded the

accuracy of judging the filling status of the whole length of fibre with aerogel core from cross-sections, thus a viewing method of aerogel core from profile side without mechanically destroying the aerogel was required.

Fig 3. 14 Different focuses on the cross-section

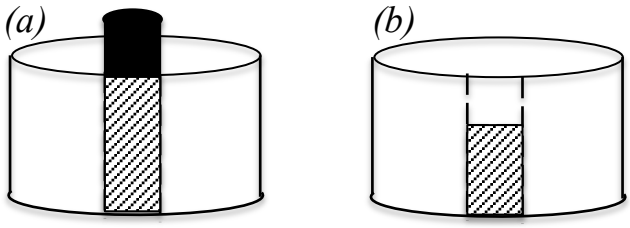

Fig3.15 Two possible outcomes after an unperfected cutting: (a) aerogel stands out of the core (b) aerogel sucks in the core.

Index matching fluid (IMF), which has a refractive index that closely approximates that of an optical fibre, is used to reduce Fresnel reflection at the surface. A droplet of IMF into one end of the fibre may provide a new examination method since aerogel and the cladding have different refractive indices. The experimental results showed that the fluid dissolves the aerogel core a little, which was not surprising inasmuch as aerogel was mainly air. However, the diffusion rate in the claddings is much faster than that in aerogel core, as shown in Fig 3.16.

Fig 3.16 Index Matching Fluid on one side of the fully filled aerogel fibre

This image presented a particularly useful assessment of testing the filling capacity: if IMF is injected into the aerogel cladding for several centimetres, the filling quality can be identified through the profile without damaging the cross-section.

A hand-held syringe to push IMF into one end of the fibre and was kept stable for 20min. A non-uniformly filled core structure which contained fully filled aerogel core and empty area inbetween is illustrated in Fig 3.17. Fig 3.18 gives a more direct vision of the filling quality through the whole length of the fibre. At the beginning, aerogel and cladding were both filled with IMF, from which we can see a 3mm empty area. Then due to the different flowing rates in cladding and aerogel, the aerogel core filled in the fibre was observed and it was very continuous for 1.5mm. However, a 1mm-long empty area appeared, this could be caused by small air bubbles in the sol that were sunk into the fibre core unintentionally when using the vacuum pump setup. Finally, for the part that IMF was not reaching, we can find an area that had both core and cladding.

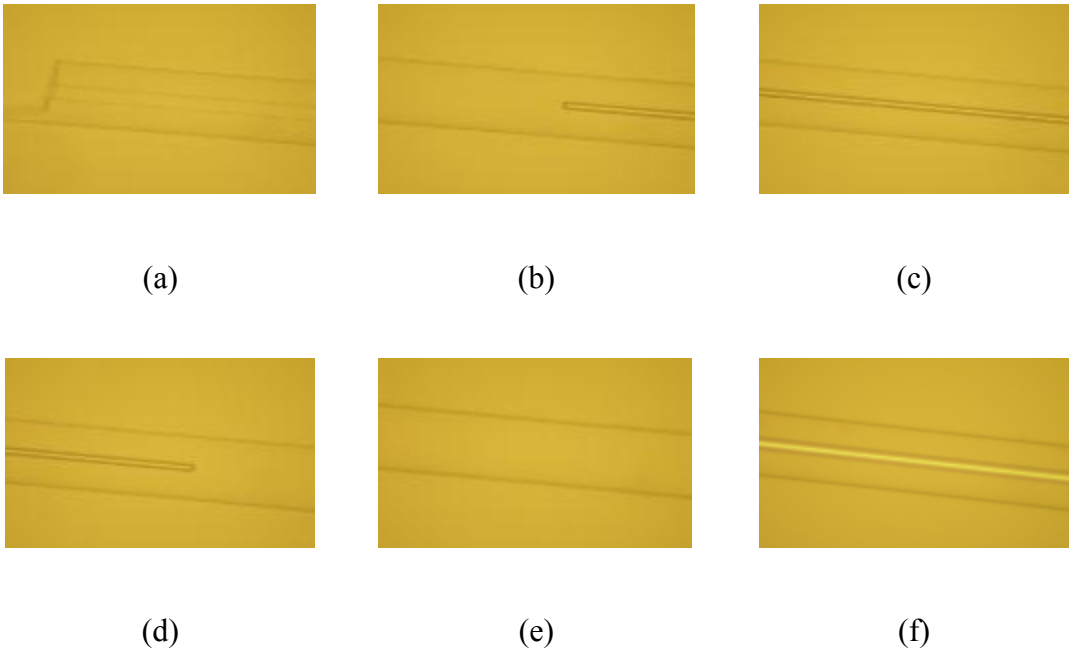

Fig 3.17 Sideways of filled aerogel fibre under microscope 50×

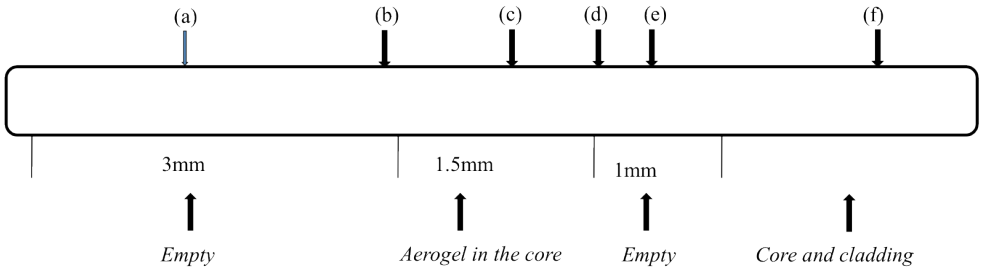

Fig 3.18 Schematic diagram of the non-uniformly filled aerogel fibre

3.4.4 Positive pressure filling

Since the vacuum pump might have produced bubbles in the aerogel, which would have dramatically increased the loss, a new positive pressure filling method was designed as shown in Fig 3.19. It consisted of a rig that held the syringe vertically, and a flat clamp to lock the position of the plunger as well as producing different pressures. The fibre was sealed to a needle tip with silicone glue. The highest pressure

that silicone glue could stand was found to be 5bar, however the sol could be discharged because of the failing of the seal at as low a pressure as 3.8bar, thus 2-3bar was chosen as the ideal filling pressure for safety and reliability.

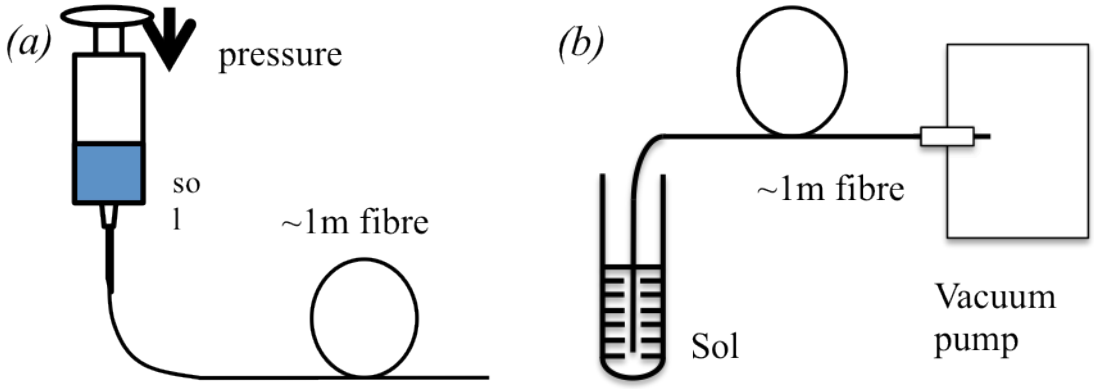

Fig 3.19 A sketch of the positive pressure equipment (a) and vacuum pump filling equipment (b)

Compared to the vacuum pump filling experiment, the positive filling method could provide a pressure difference larger than 1bar. According to Hagen-Poiseuille equation, the volume flow rate Q can be written [4]:

$$Q = \frac{\pi r^4}{8\eta}\frac{\Delta p}{L} \tag{3-5}$$

where r is the internal raidus of the tube, Δp is the pressure difference between the two ends, η is the dynamic fluid viscosity and L is the length of the tube, as seen in Fig 3.20.

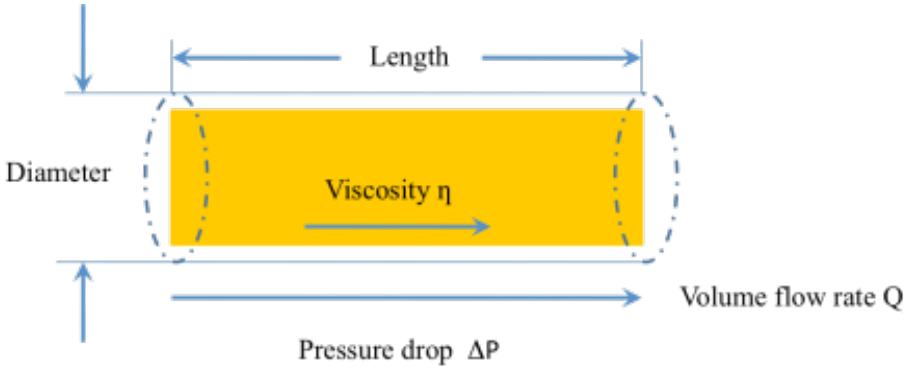

Fig 3.20 Schematic diagram of Hagen-Poiseuille equation

The gel flows into the fibre much quicker with a higher-pressure difference, which meant this design shortened the filling time. This was tested through a hollow core bandgap fibre with a core diameter of 10μm that worked at visible wavelength and a He-Ne laser (633nm) was coupled to the other end of the fibre. The red dot appeared at the interface of sol and air, which indicated the filling length. Fig 3.21 shows an experimental result of the relationship between the filling time and length. The filling length increased at a remarkably fast rate during the first five minutes and climbed all the way up with a decreasing acceleration rate. This result produced a significant data of filling fibres with different cores, as the flow rate was in direct proportion to r^4. As for filling with doped aerogels, a shorter gelling time which is slightly larger than the filling time caused a more uniform gel or aggregation of the doped particles.

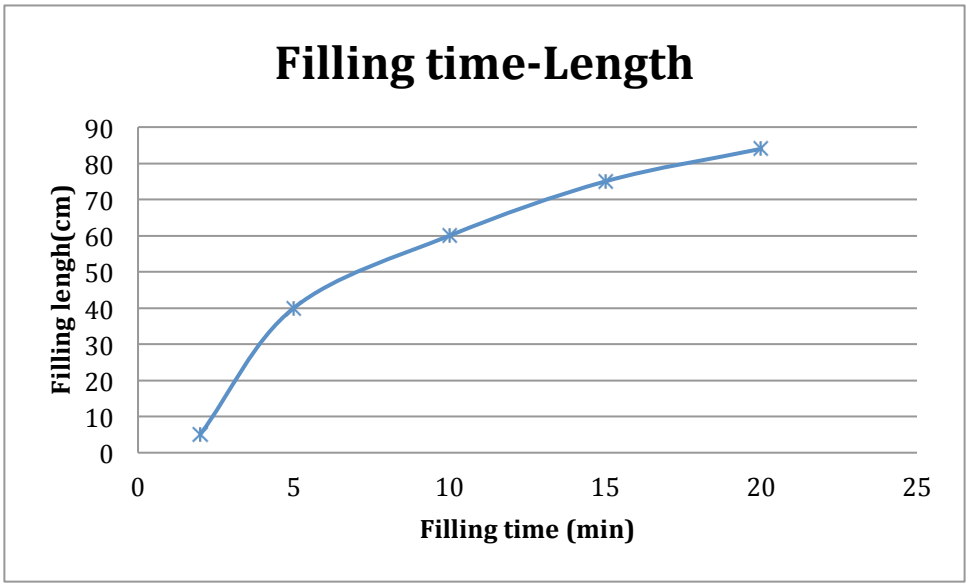

Fig 3.21 The relationship between filling time and length at 2bar

Another advantage of positive pressure filling was that one side of the fibre is free, which provides the opportunity to determine the filling time by observing the free end. Fig 3.22 and Fig 3.23 shows the observations of the end of fully filled fibre by microscope and USB microscope respectively.

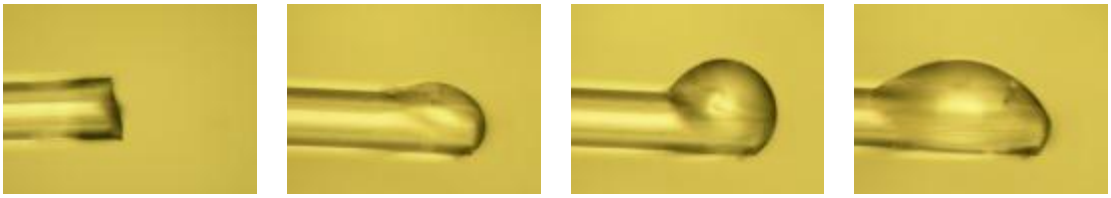

Fig 3.22 The free end of TIR fibre under microscope 50×. It was quite clear that a drop formed at the free end of the fibre when it was fully filled

Fig 3.23 The filling end of TIR fibre under USB microscope

To summarise, the positive pressure method has the potential in filling aerogel fibre as the pressure control and filling time is superior to the vacuum pump filling method. It is possible to observe the exact time at which the fibre has been completely filled with sol, as an excess droplet exits the open end of the fibre. Also, this method can be used in many liquid filled equipment setups and have potential with some sols that may gel in a short time.

3.5 Conclusion

We have demonstrated a waveguide with an aerogel core, with a single round cladding fibre to provide a cladding with an effective refractive index low enough to confine light by total internal reflection. There are many possibilities for further study of aerogel-filled waveguides, for example the waveguide property with doped aerogels. The positive filling set up can improve the efficiency of the liquids filling

hollow core fibres and the index matching fluid can be used to examine the filling capacity from the side view of fibres, which is also a promising method that requires further research.

Chapter 4 Sol-gel derived thin film

4.1 Introduction

Behaviour of the aerogel as a waveguide has been discussed in the previous chapter, while for some applications aerogel or xerogel thin films are required. Low-loss deposition of sol-gel derived silica films on tapered fibres was carried out by G. Kakarantzas in 2004 in our centre by using TEOS as precursor and HCl as acid catalyst, in which he demonstrated the manufacturing of a structural long-period grating that produced the layer with variations in refractive index [12]. Additionally, there are publications on the coating of silica film around a fibre to produce a gas sensor or humidity sensor [34,35].

In this chapter, a crack-free film produced by dip coating with a refractive index of about 1.30 has been demonstrated after investigating optimum coating time and aging time.

4.2 Selection of coating methods

Different coating methods contribute to different substrates and parameters of films. C. J. Brinker and L.W. Hrubesh had an overview on the coating methods of making sol-gel derived film [4]. Here some basic concepts and typical thicknesses produced by three common processes namely dipping, spinning and spraying are discussed to provide a general overview of coating procedures [36].

4.2.1 Dip coating

This process is used only when an entire surface of the substrate is to be coated. Using this method, films thinner than a few microns can be produced depending on the viscosity of the precursor and the withdraw rate.

4.2.2 Spin coating

Spin coating is normally used in semiconductor coating. It was performed with a spinner which was entirely contained within an enclosure that had a solvent saturated atmosphere. Film thicknesses of less than 2μm were obtainable.

4.2.3 Spray coating

This process is used to coat thicker single layers on substrates like glass and silicon wafers. Films as thick as 80μm have been achieved with this method. An aspirator is used in this process to spray the precursor solution directly onto the substrate, which is then held in a nearly vertical position to be further drained by gravity.

In the research of silica film coating on an optical fibre with an axially and radically symmetric cylindrical shape, the dip-coating process is considered the most convenient and efficient way. Fig 4.1 is the schematic diagram of dip coating. A droplet of sol suspended at the tip of a syringe needle is translated along the fibre at a constant speed. The moving liquid trails the fibre in a fluid mechanical boundary layer covering the surface and repetitive motions are applied to produce thick films.

Surface preparation was an integral part of a successful protective coating. A razor blade was often used to remove the coating while acetone was used to clean residues from the bare fibre as it was easily evaporated and did not leave residual chemicals on the substrates. Then the fibre was fixed to the designed holder and placed in a methanol vapour that was created by the evaporation of 20ml of methanol in the container and 2ml of methanol in the holder prior to film deposition. The preparation system is illustrated in Fig 4.7.

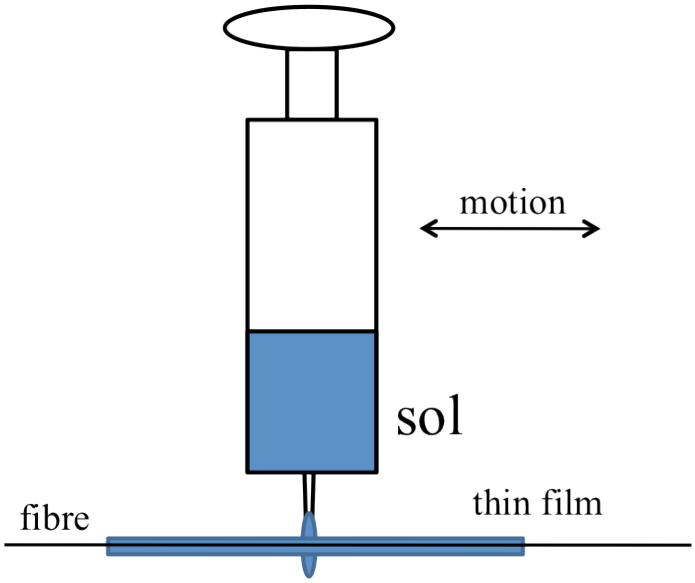

Fig 4.1Schematic diagram of the modified dip coating process

4.3 Gelling time and crack prevention in thin film coating

Though the coating method is similar to that of G. Kakarantzas, the design of experimental facilities to produce a crack-free film remains challenging. Two research questions will be presented in this section.

4.3.1 Determination of the gelling time when the sol is contacting the fibre

The gel time of sol and the coating start time are two major factors in the preparation of a film to guarantee its uniformity and repetitive producibility. The initial idea is to separate the catalyst from the sol but it evaporates as a vapour surrounding the fibre. This scheme possibly ensures that the sol converts into gel exactly when it touches the fibre. Thus a separated precursor containing TMOS, methanol and water with molar ratio of 1:3.6:4 (volume ratio 2ml: 2ml: 1ml) was utilised.

$$Si(OCH_3)_4 + 2H_2O \rightarrow SiO_2 + 4CH_3OH \quad (4\text{-}1)$$

TMOS: water ratio is particularly important and is intended to be more than the 1:2 stoichiometric molar ratios in this experiment so that all TMOS hydrolyses to silicic acid. By separating the catalyst from precursor, the mixture of TMOS, methanol and water was inhaled into the syringe, then 5ml of 2.0M ammonia/methanol (catalyst) solution was added into the container without immersing the fibre, which assumed that the sol only starts to gel when the drop has been pushed out from the syringe. After four sweeps of the syringe, the surface of the fibre was expected to affix with a film. Surface images of the films are shown in Fig 4.2.

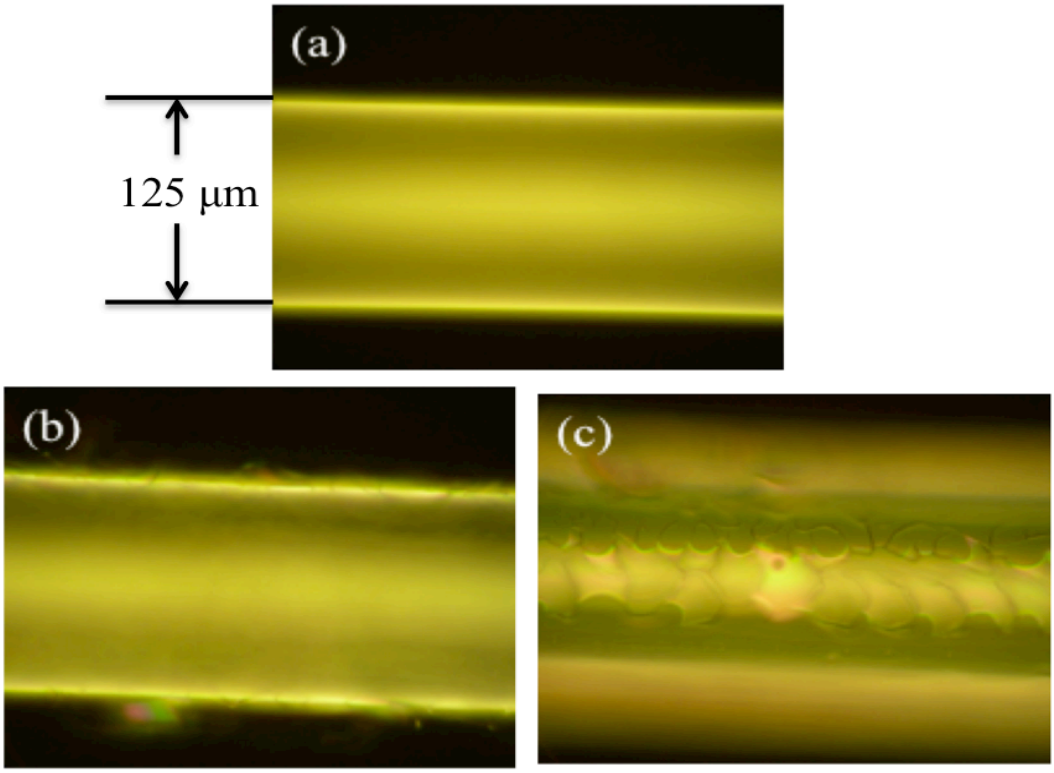

Fig 4.2 Photograph of (a) bare fibre. (b) Wet gel thin film seen under the microscope focused on the edge. (c) Focused on the surface. All of the images were taken using 50×magnification

The contrast between the clean fibre after removing the coatings and coated fibre was significant: the coated fibre (b) has isolated patches that seemed like a flaking cracked film. By focusing on the surface of the coated fibre, interference fringes were visible, which indicates that there was a thick cracked film at the point where the fibre and

droplet contacted.

As the ammonia concentration was difficult to control and measure after pouring into a container, it made the experiment less repeatable. Moreover, ammonia was a potential health hazard, so in order to obtain precise control of the chemical reaction, the base catalysed sol was applied in the following experiments and investigation of the optimum coating start time and aging time will be presented in a later section.

4.3.2 Crack prevention

As described in Chapter 2, cracks change the network of the micron-sized skeletons and cracking should be avoided for a successful sol-gel processing. However, in the results shown above, cracks can be viewed as good evidence of film residue adhesion to the fibre, since sometimes there was no evidence of coating on the fibre after the coating process. The next research question was how stop the film from cracking since both aerogel and xerogel films required crack-free wet gel films before supercritical drying or ambient drying.

The reason why the wet gel cracked has been discussed in detail in Chapter 2. It is caused by capillary force from the meniscus between liquid and solid skeleton. To reduce the influence of capillary force, a transparent plastic bag acting as a glove box was used inside which sufficient methanol is added to create a saturated vapour and in principle this could prevent the wet gel film from cracking as the meniscus interface would be stable in a saturated environment. In addition, methanol is also required to be poured into the fibre holder. This would prolong the existence of a saturated atmosphere to reduce the possibility of cracking when the fibre is examined under the microscope. Also, the gelling point and aging time may contribute to the cracks, as the wet gel becomes stronger during the aging process. These aspects will be examined with the solution of Section 4.3.1 as well.

4.4 Experimental design of thin film coating

4.4.1 Holder design

The holder used for depositing sol around a tapered fibre had a significant impact on the whole fabrication process. The structure of an initial holder is shown in Fig 4.3. A removable base was used to increase the diffusion area during supercritical drying. However, the active conjunction between the holder body and the base impeded the coating experiment with less controllability since the evaporating time was altered due to the methanol leakage from the joints. The 20mm depth of holder was still a reliable design as the fibre would not contact the liquid methanol in the holder. The holder for thin film coating has a simple shape, as shown in Fig 4.4.

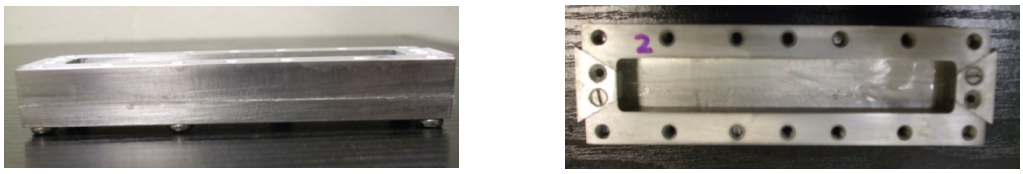

Fig 4.3 The side- and top-view of the holder with a body-and-base design

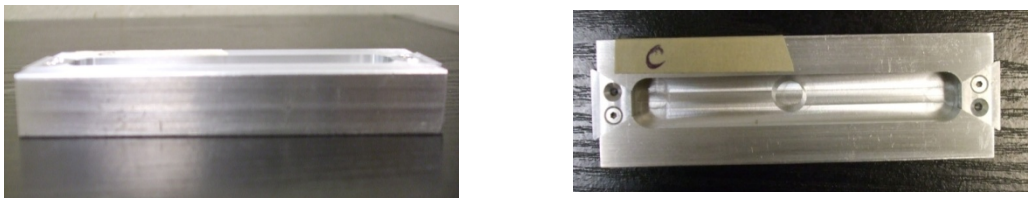

Fig 4.4 The side- and top-view of the holder with a monolithic design

4.4.2 Clamp design

In the initial design, a clamp held the syringe vertically and it moved with the stage after a droplet was squeezed (seen in Fig 4.5(a)). Surprisingly, sometimes the droplet at the tip of the needle may shrink back into the syringe instead of falling down due to the force of gravity: one possible explanation is that when the plunger of the syringe was pressed, the air in the syringe was compressed and that can push the liquid out of

the needle to form a droplet; on the other hand, it could also push the plunger because the cross-sectional area of needle was very small and was likely to provide larger resistance. To tackle the problem a flat and fixed-top clamp with screw thread was designed to ensure a precise and stable control of the syringe (seen in Fig 4.5(b)).

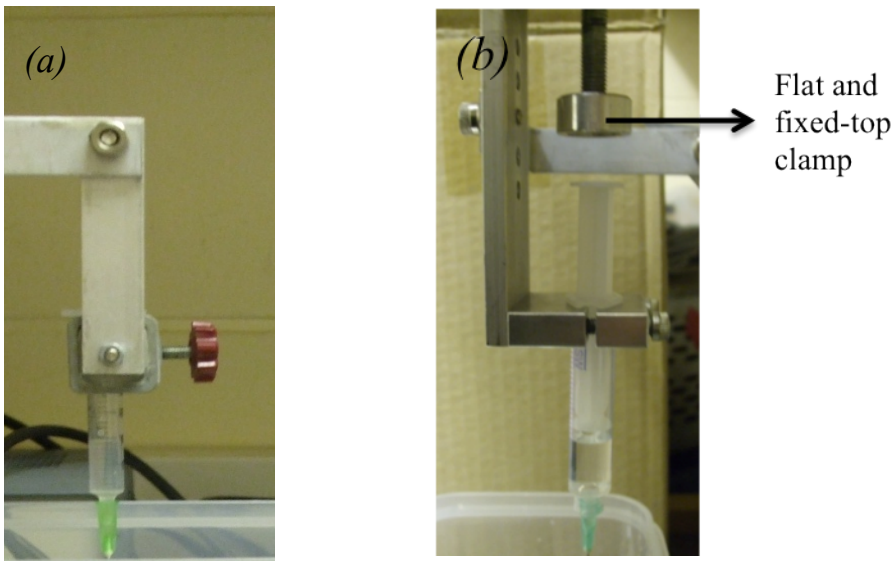

Fig 4.5 Clamp design: (a) initial design. (b) Flat-top syringe holder with screw thread to push the plunger

4.4.3 Coating equipment

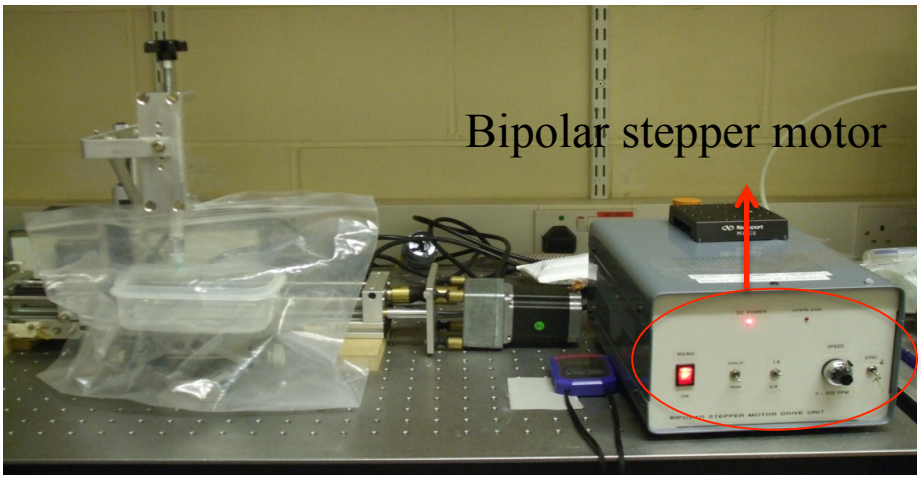

Fig. 4.6 A photograph of the dip coating process rig

The speed of the dip coating process was controlled by a bipolar stepper motor and the fastest speed was 30s per round-trip sweep (Fig 4.6). The plastic bag acted as a protective cover to contain the methanol atmosphere and to protect the wet gel film from cracking as discussed in Section 4.3.2. Inside the bag there was a syringe, a plastic container, a clamp and a lab jack (Fig 4.7). The clamp held the syringe and was mounted on a motorised stage, which moved along the orientation of the fibre. The fibre holder was mounted on the container with liquid methanol. The lab jack was used to adjust the distance between the tip of the syringe and the bare fibre. Fig 4.8 illustrates a close-up picture of the coating procedure; the number of passes of the sol drop was determined by the required thickness of the film

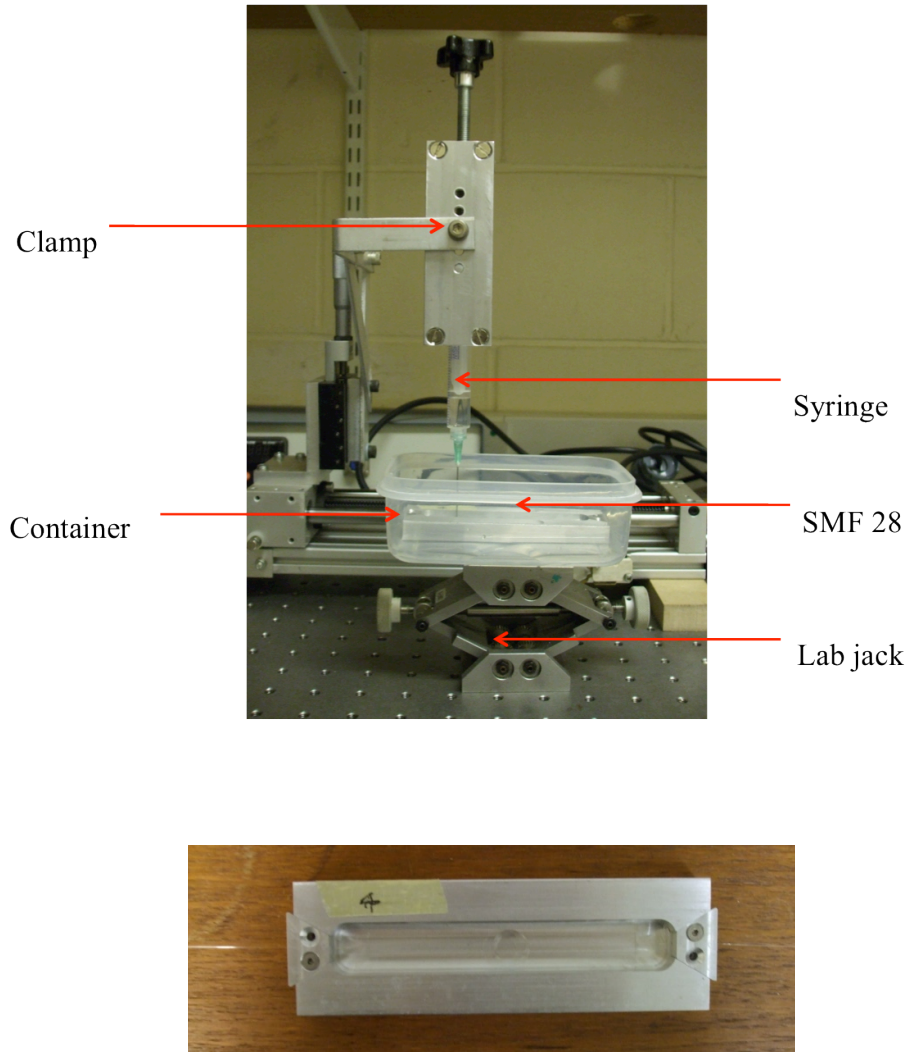

Fig 4.7 A photograph of the dipping process setup in the bag

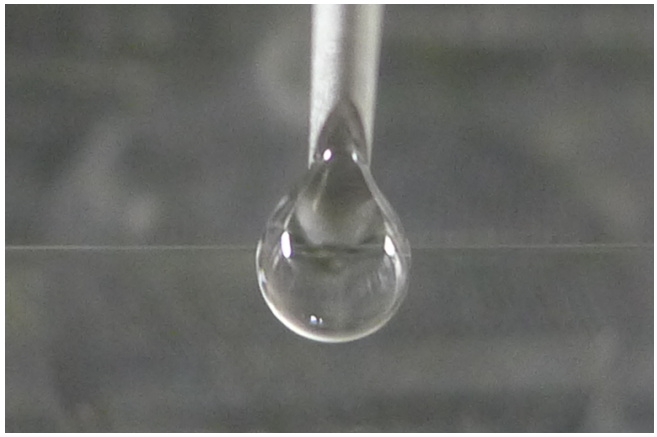

Fig. 4.8 A photograph shows the drop on the fibre surface.

4.5 Results and discussion

In this section, more detailed mechanisms in the sol-gel process for thin film coating are discussed and a series of tests on the films are described.

The chemicals were combined into sol and thoroughly mixed, then agitated by shaking in the test tube several times to create a more homogeneous wet gel on a macroscopic scale, followed by the sol being drawn into the syringe. After only a single sweep of the dip coating process, the film was kept in the methanol environment that prevented evaporative drying by reducing the meniscus caused by wetting forces at the sol-air interface and then the film was aged for 12 hours. After that, a uniform, crack-free film was formed and there seemed to be no difference compared to a clean fibre without film that had been aged in methanol atmosphere for 12 hours. In Fig 4.9, (a) was the smooth surface of clean fibre that aged in methanol atmosphere for 12hrs, after scratching by a razor, only line trail was appeared(c). While for the fibre with thin film coating, it was also shown smooth surface after aging in methanol atmosphere for 12 hrs (b), however, after scratching the surface, minor flacks were observed to prove the existence of the film (d).

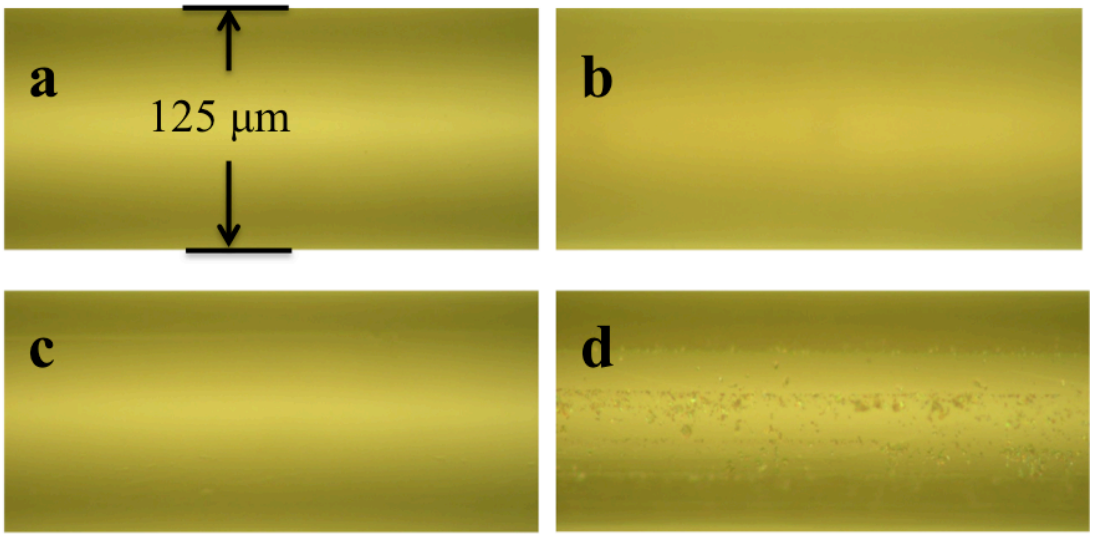

Fig 4.9 The surface of clean fibre (a,c) and crack-free thin film (b,d) after being treated in a methanol atmosphere for 12 hrs before and after scratching with a razor

In order to improve the repeatability of the film deposition, both the optimum processing times of coating start time and aging time were tested since they were determinative on the film quality. As the thickness of the film was significantly smaller than the diameter of the fibre, the diameters of the coated fibres were approximately 125μm. All the time scales of crack formation used in the following chapters started from 5min, this is because it took about 5min to move the samples from the thin film deposition room to the measurement room.

4.5.1 Test of coating time

Coating time or starting time was when the droplet made contact with the fibre and followed by an even speed translation. The recipe used in this experiment had a gelling time about 8-10 minutes. Before the coating point, the sol was held in the syringe; after coating, the fibre was immersed in a methanol atmosphere, which suggested the catalyst ammonia was diluted. Presuming the gelling time of the sol in the methanol atmosphere was approximately 10min, the coating time was divided into minute intervals for test. As for the viscosity of the sol, it dominated whether the

droplet was suspended on the tip of the needle or dropped down by gravity. It was found that usually after 4.5min the droplet could stay still for a single sweep that lasted 30s, so that the time scales were chosen from 5min to 8 min and the results of the film quality inspection are shown in Fig 4.10.

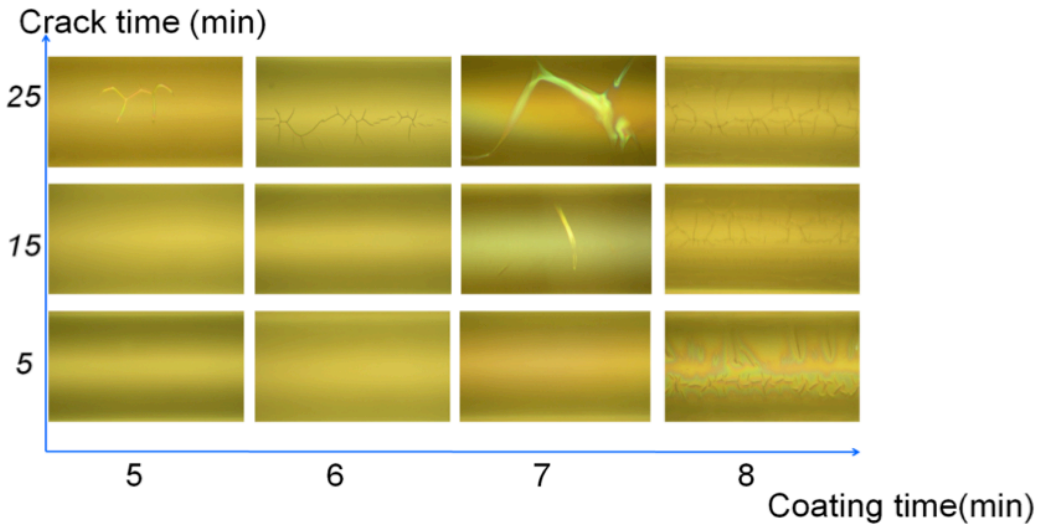

Fig 4.10 The correlation between crack time and coating time. An optimum window was found at 5-7mins of coating that ensured the cracking occurred after 15min.

The graph indicates that uniform and crack-free films could be formed using a coating time between 5 to 7mins. This may be because whenever coating start time was close to the gelling point, the sol would be too sticky to form a thicker film that was likely to crack due to large capillary force. To conclude, the optimum coating window was 5-7 min and shorter coating time has longer cracking time.

4.5.2 Test of aging time

Wet gel films require time to age before the drying process. During the aging process, wet gel can convert to more rigid structures. In order to seek the best aging time to fabricate uniform and crack-free films, coating times of 5min and 7min have been studied.

As shown in Fig 4.11, after an undisturbed aging process for about 12hrs, the fibres

with a coating time of 7min had only slight cracks however more significant cracks were formed after 20min's exposure in the air. In contrast, coatings with a processing time of 5min did not change after 20min, but small flakes appeared after using an acetone-cleaned razor to scratch the surface. In conclusion, the films produced with coating time starting at 7min cracked after 12hrs aging time in methanol vapour while those starting at 5min did not.

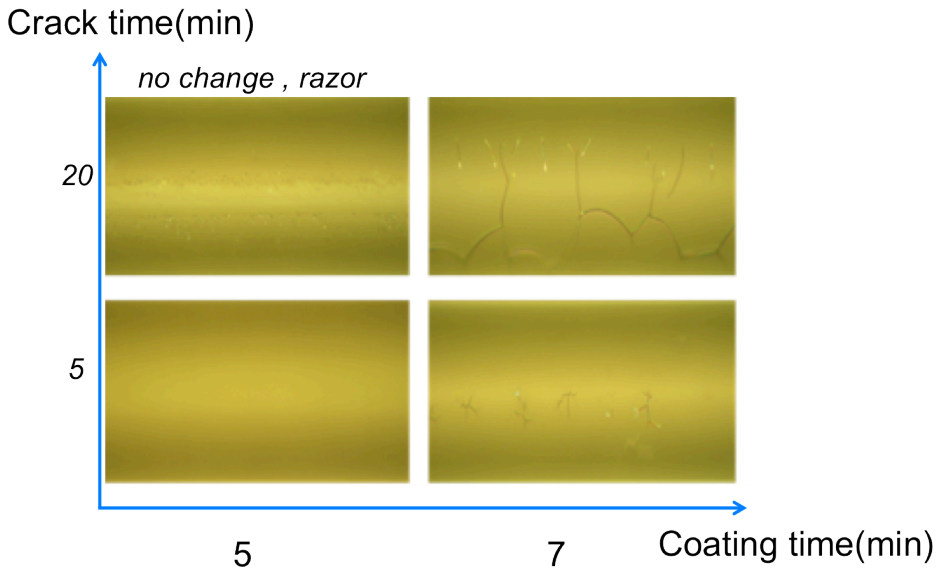

Fig. 4.11 Appearance of the coating that had been left in the methanol atmosphere for 12hrs. "No change, razor " means there was no change to the surface and the image was taken after using razor blade to scrape the surface, which will be used in following images as well.

An aging time of 60hrs gave the results as shown in Fig 4.12. Insufficient methanol vapour caused more cracks on the 7min wet gel films. However, there was still no change in those with coating time at 5min. Even though the coating time from 5min ensured a crack-free film after aging for 60hrs, in order to get more flexibility for the fabrication of crack-free films, 12hr would provide a wider range of choice for other coating times. To summarise, longer aging time in methanol vapour caused more cracks on the film that was fabricated with a 7min coating time, while for the 5min coating time, the film was still crack-free.

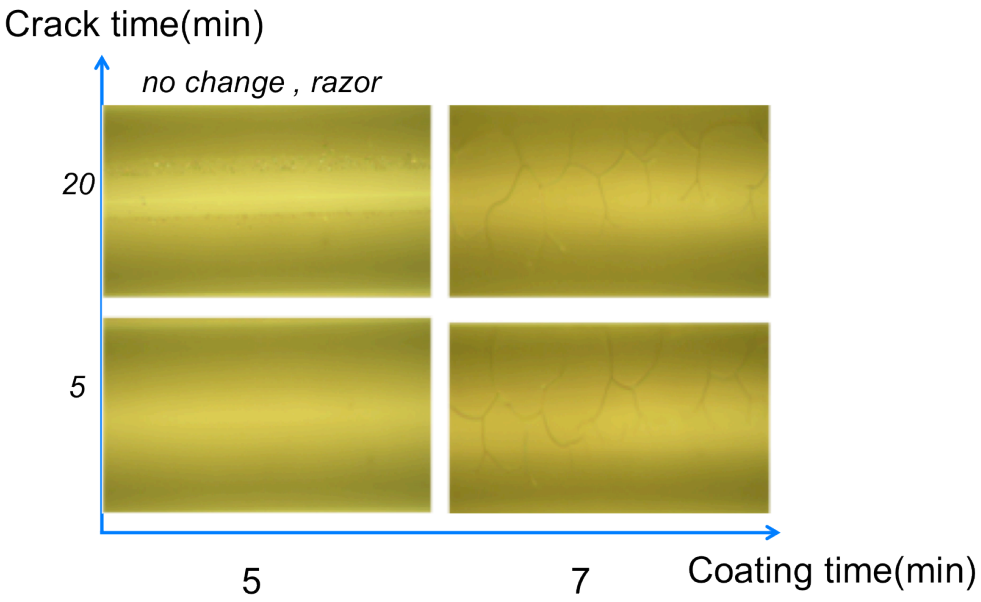

Fig. 4.12 Appearance of the film that had been aged in the methanol atmosphere for 60hrs

4.5.3 Test of aging process

It was known that the aging process could also be conducted by immersing the fibre in methanol, thus contrast experiments between different aging times and environments are demonstrated in Fig 4.13. There are three different aging processes: exposure in air (as the control experiment), aging in methanol atmosphere and aging in pure liquid methanol. The results implied that there was little difference between the film quality by either aging the film in methanol atmosphere or pure methanol. The wet gel film cracked immediately after an exposure to air and also the cracks grew with time.

Until now, we have found that wet gel film would crack when exposed in the air, but both of the two aging methods in either methanol vapour or pure methanol liquid seemed to show no difference. Possible explanations are: the physical properties of the wet gel film might have been changed after the contact with methanol for a long time and the methanol in the holder might also alter the structure, which requires further exploration. In conclusion, aging in both vapour and liquid methanol ensured

the crack-free property while the absence of methanol caused cracks almost immediately.

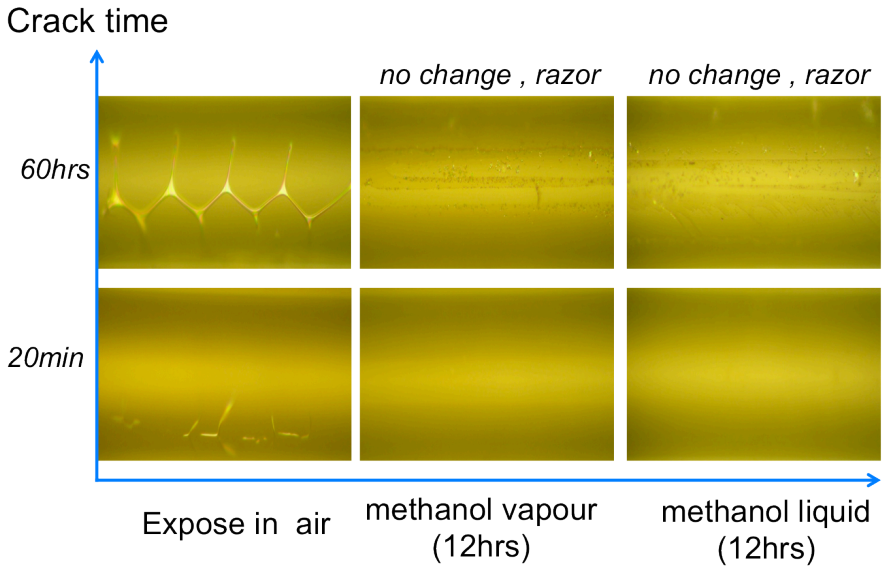

Fig 4.13 The influence of different aging times on the quality of thin films that with coating time 5.5min.

4.5.4 Tests of different methanol protections

Since both vapour and liquid methanol protected thin film had the same quality after 12hrs aging time, we are interested if those films are still crack-free after a rapid liquid evaporation. Wet gel film can be distinguished from other films by the occurrence of cracks when the liquid in the pore evaporates quickly. A hot air gun was used to evaporate the methanol liquid rapidly, usually in a few seconds. The results showed that samples left in the methanol vapour for 12hrs did not suffer any crack or shrinkage and flakes appeared after a scratching with a clean razor blade. Those films that immersed in liquid methanol presented flakes rising from cracks after the fast evaporation by hot air gun. To conclude, the films that were aged in methanol vapour for 12hrs did not crack after rapidly evaporation, while some of those films aged in methanol liquid suffered cracks which might suggest that wet-gel

film had been deposited.

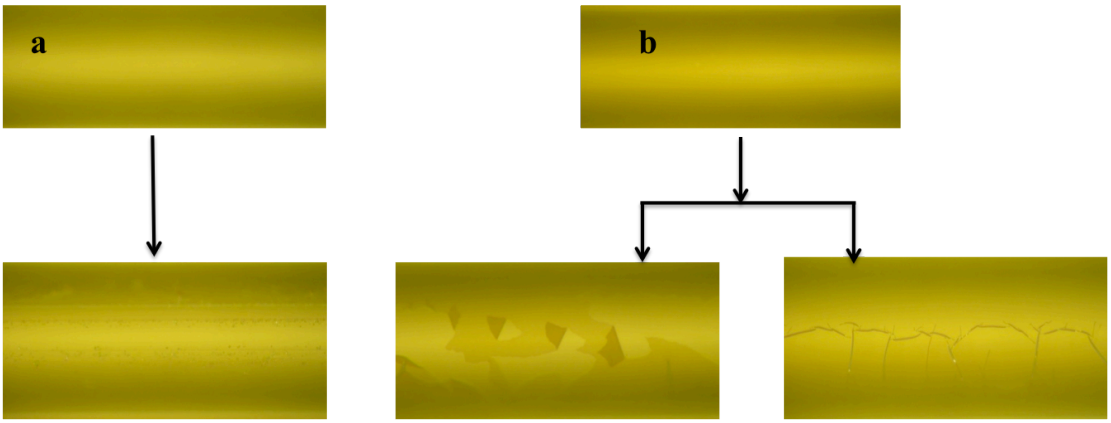

Fig 4.14 Outcome of hot air gun test. (a) The film aged in methanol vapour remained crack-free, yet flakes could be seen after scratching with a razor. (b) Aging in pure methanol wet gel test by using hot air gun led to the formation of cracks and flakes.

4.5.5 Surface Modifications

As discussed in Chapter 2, normal aerogels or xerogels are hydrophilic, thus the crack-free films are expected to be hydrophilic and the structure will be likely to be destroyed after contacting with water. The test was conducted using distilled water to prevent the interference of impurities. The image of water-damaged surface is shown in Fig 4.15.

The surface is able to be changed into hydrophobic if the wet gel film is washed in hexamethyldisilazane ($(CH_3)_3SiNHSi(CH_3)_3, HMDS$) as HMDS will break down chemically to become TMS and ammonia. After 12hrs aging in methanol vapour, the film was immersed in a mixture of HMDS and methanol with a volume ratio of 1:4. The HMDS process was adequate to ensure hydrophobicity and Fig 4.16 illustrates that smooth surface was formed by washing the films in HMDS for 24hrs. Although visible cracks appeared on the surface of some of the fibres, most of the films

remained uniform and crack-free (Fig 4.16(a)), or sometimes with tiny cracks just beyond the drop of water (Fig 4.16(b) and (c)).

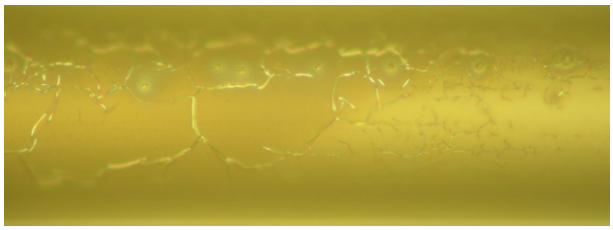

Fig 4.15 The surface of hydrophilic film after water evaporation.

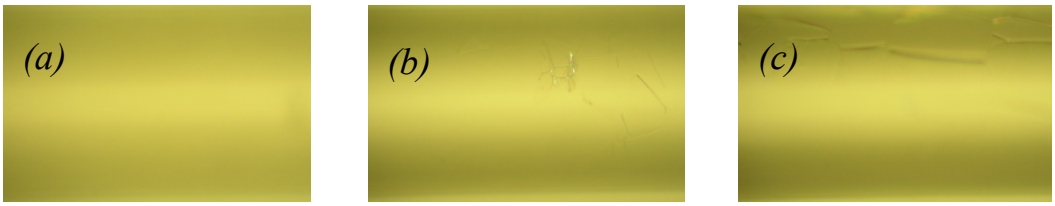

Fig 4.16 The surfaces of HMDS hydrophobic film after the water evaporated.

A key parameter to characterise the hydrophobicity is contact angle, which is conventionally measured where a liquid/vapour interface meets a solid surface [37]. The contact angles of non-treated, MTMS-treated and HMDS-treated films were measured to be 30°, 50°and 120°, respectively, as illustrated in Fig 4.17. It was then proven that the HMDS treatment was a more effective method than MTMS treatment to increase the hydrophobicity of the film.

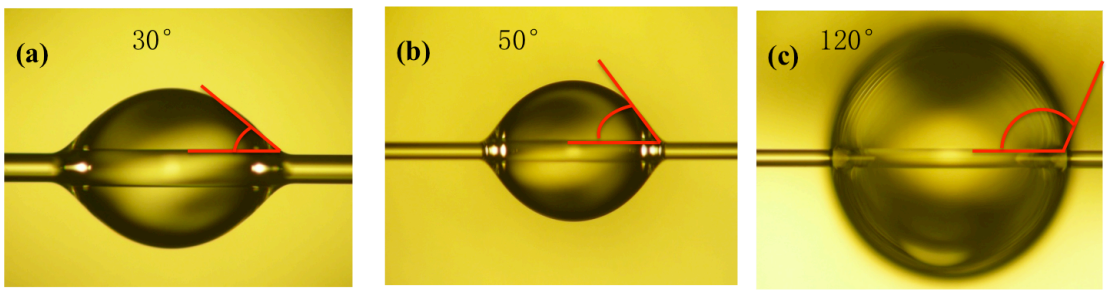

Fig 4.17 Distilled water drops on (a) untreated surface, (b) surface treated with MTMS and (c) surface washed in HMDS. Contact angel θ=30°, 50°and 120°, respectively.

4.6 Characterisations of silica film

Until now, a crack-free thin film was successfully coated on a fibre; however, the thickness and refractive index of the film itself were still unknown. SEM and TEM were used to investigate the microstructure of the film around the fibre. As for refractive index, a repeatable result was obtained by making thin film on SiO_2 substrate using an ellipsometer.

4.6.1 SEM measurement

A scanning electron microscope (SEM) provides images containing information about the sample's surface topography and composition. By scanning the sample with a focused beam of electrons, atoms in the sample interact with the electrons, producing various detectable signals [38].

In order to measure the thickness of the crack-free film, the cross-section of fibre was observed under SEM (JEOL 6480LV). The film was coated with Au to prior to SEM to increase its conductivity. Fig 4.18 indicates a ring-shaped thin layer around the fibre with an approximate thickness of 600nm. The surface of the deposited was proven to be smooth even under a micron-scale observation, which indicated the good quality of the coating presented in the previous experiment. The flakes which appeared at the edge of the fibre might have been caused during the fibre cleaving.

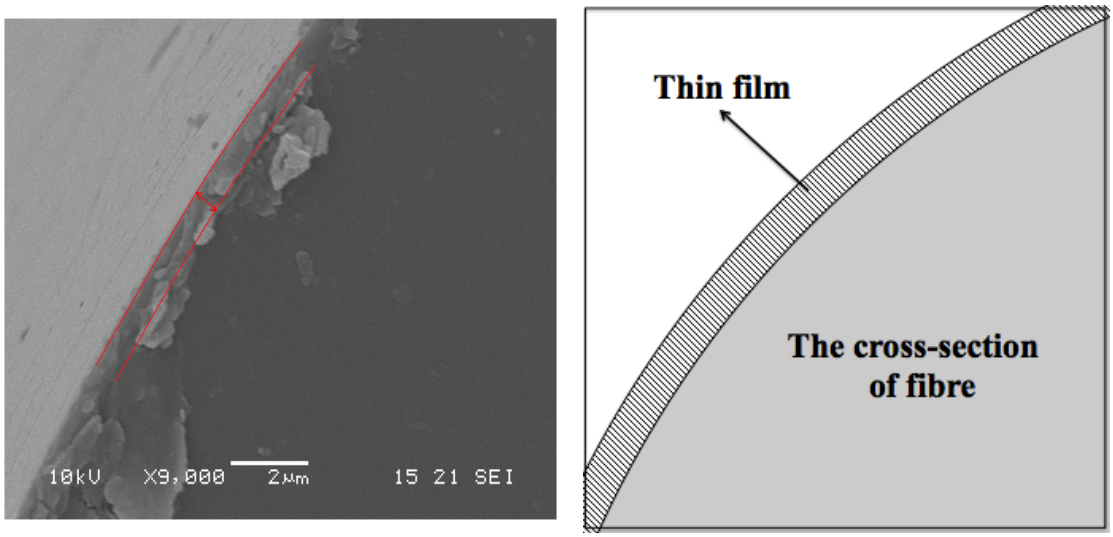

Fig 4.18 SEM image of cross section of crack-free film

4.6.2 TEM measurement

TEM measurement provides images through a beam of electrons that is transmitted through a thin specimen and interacts with the specimen when the beam passes through [39].

As the film was not easily peeled from the fibre, 12 fibres were coated with thin films after an aging time of 12 hrs and then a razor was used to scrape the films to prepare the TEM specimen. Meanwhile, aerogels that were made by the same recipe were examined as a control experiment. During the preparation of the specimens, it was found that silica aerogel has much stronger structure than silica thin films. When observing through the TEM (JEOL JEM 1200 MKⅡ; camera : GATAN DUAL VIEW 300), for the silica film, we looked into the fragment of a continuous piece in transmission light, and as we can see from Fig 4.19, a condensed region (dark part) occurred which might suggest the aggregation of silica clusters while aerogel had a more open-network structure. The bright part in Fig 4.19 indicates transparent area, which means it could be the air holes of the material while the dark part could be the silica particles. Since both the xerogel and aerogel images were the same

magnification, the darker part in xerogel film may suggest denser particles of silica.

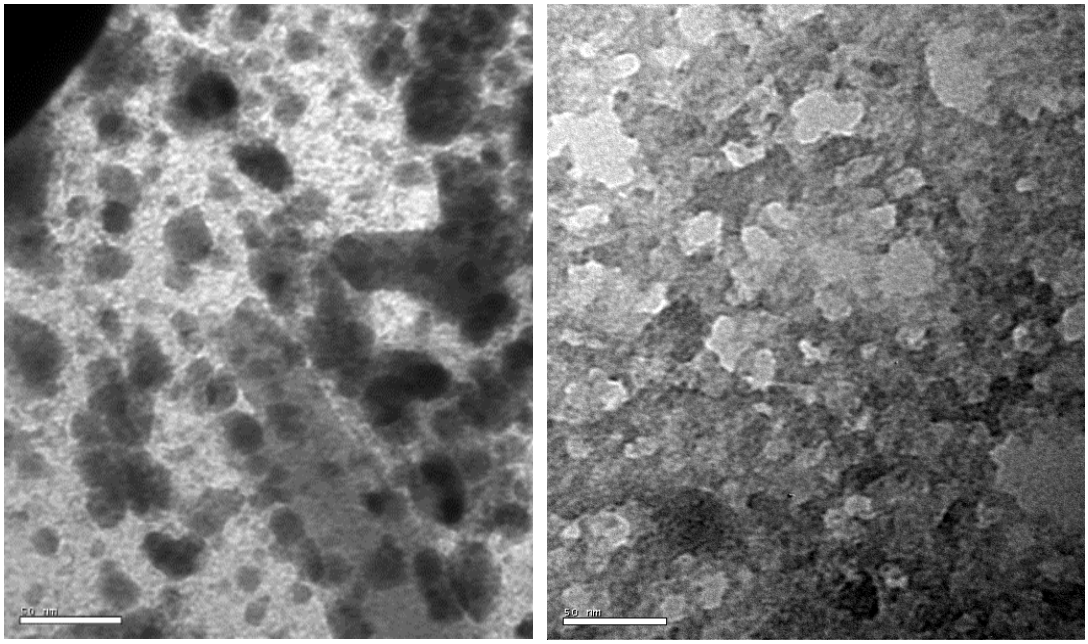

Fig 4.19 TEM image of crack-free film (left) and aerogel (right), scale bar: 50nm The bright part were air holes in the materials, while the dark part were the silica particles.

4.6.3 Ellipsometry measurement

As the refractive index of the film coated on the fibre is difficult to measure, we fabricated a thin film by dip coating on a flat silica substrate with all the procedures the same as that on a fibre. Though it was not a direct measurement on the films deposited on the fibres, as two measurements demonstrated above, it still gave us representative data of the refractive index of silica film coated on fibres.

The basic principle of ellipsometry is shown in Fig 4.20. Electromagnetic radiation from the light source is polarised by a polariser. It passes through a compensator (optional) and is reflected at the surface of the sample. After that the radiation passes a compensator (optional) and a second polariser, which is called an analyser, and goes into the detector [40]. Ellipsometry measurement provides the complex reflectance

ratio ρ of a system, which may be parametrised by the amplitude component ψ and the phase difference Δ.

$$\rho = tan(\psi)e^{i\Delta} \tag{4-2}$$

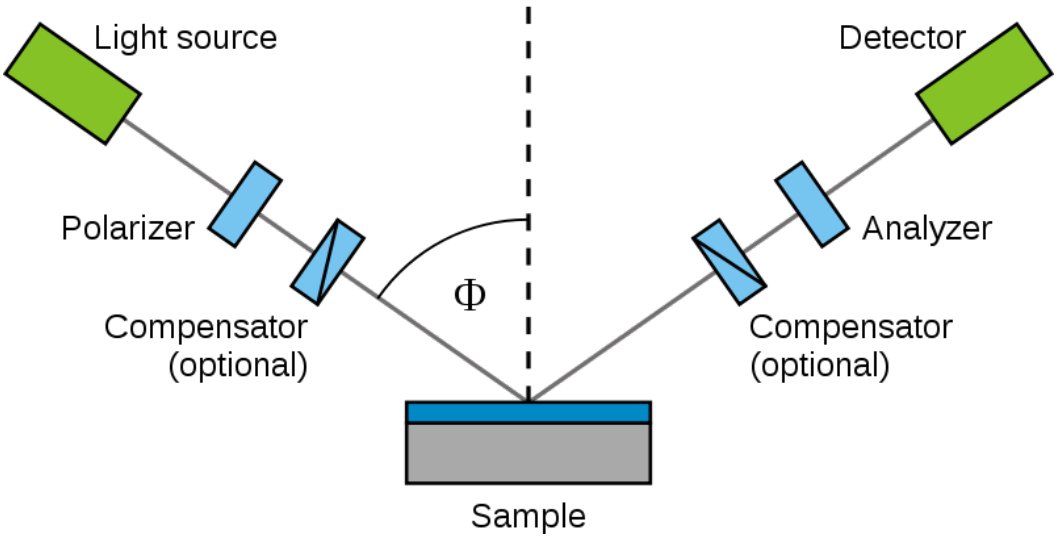

Fig 4. 20 Schematic setup of an ellipsometry experiment [41].

The thickness of the thin film and refractive index were measured with an optical ellipsometer [alpha-SE Ellipsometer from J.A. Wollam Co], equipped with a He-Ne laser with λ=633nm as the light source. The data was collected at three incident angles of $30°$, $60°$ and $75°$ and was analysed by the model of glass with transparent film. The result shows the thickness was 667.9 ± 6.867nm with a refractive index of 1.306 ± 0.0098. The thickness of the film coated on the flat silica substrate was in a good agreement with the thickness obtained in the SEM test on the coated fibre.

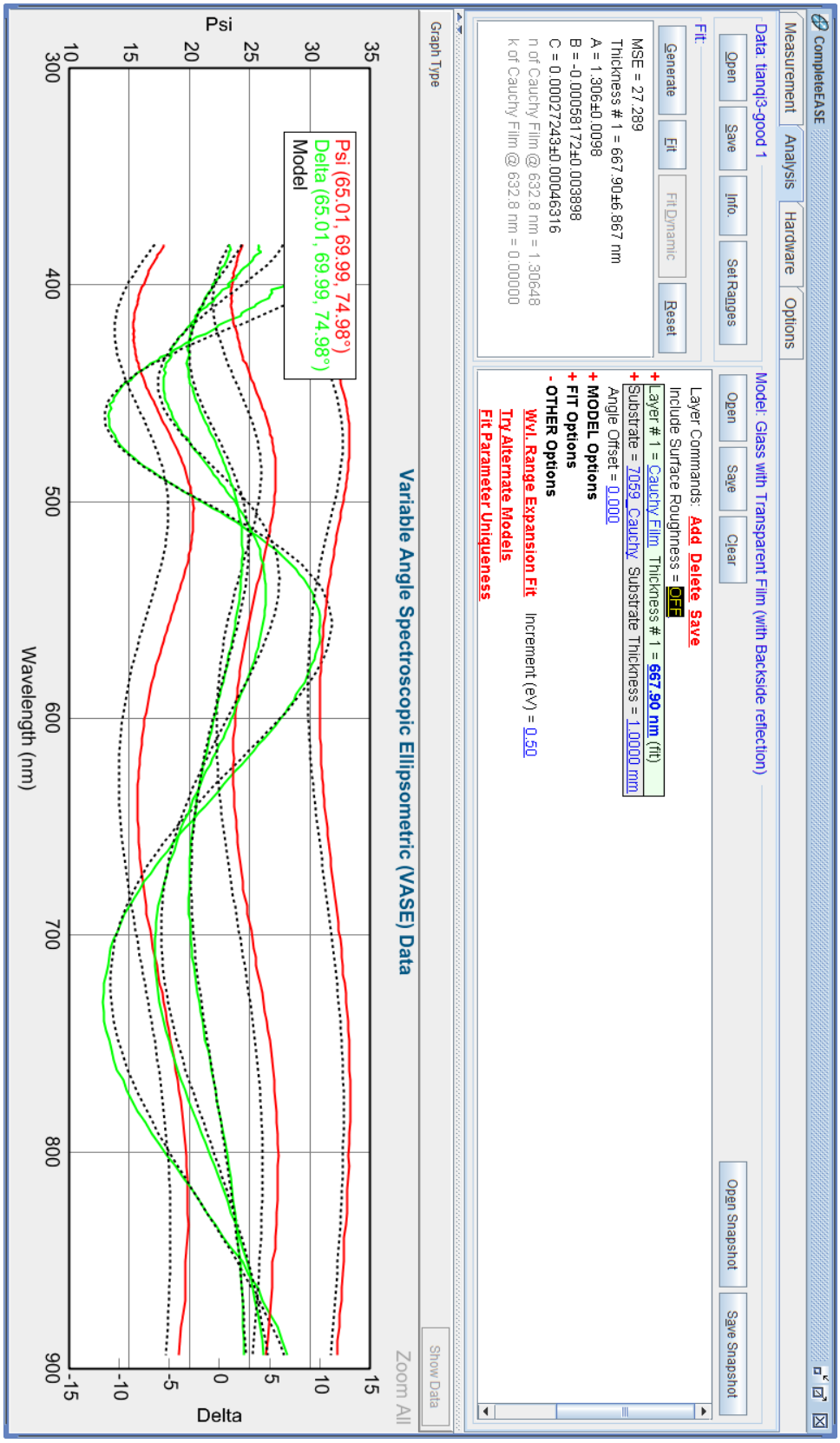

Fig 4.21 A screen shot of the measurement of a silica film produced with a coating time of 5.5 min and aged in methanol vapour for 12hrs.

4.7 Conclusion

To conclude, an experimental setup for thin film coating was developed and it was able to deposit a uniform, crack-free silica film after aging in methanol atmosphere for 12hrs. To improve the repeatability, optimum coating and aging times for the fabrication of a smooth film were demonstrated. Several hydrophobic treatments have been tested and results showed that HMDS could improve the surface hydrophobicity better than MTMS treatment. The thickness of the crack-free film was about 600nm measured through SEM. The nanostructure of crack-free film was also observed by TEM compared with that of aerogel that was fabricated from the same recipe. Images illustrated that the crack-free film has denser silica particles and less porosity than aerogel. After using the same recipe to produce film on silica substrate, the refractive index was measured to be 1.30.

Chapter 5 Evanescent-wave coupling

5.1 Introduction

Evanescent waves are near-field waves coming out of the fibre-air interface when light travels through a fibre via total internal reflection due to the continuity of the electromagnetic field at the boundary. Light could be transmitted from one fibre to another by means of evanescence, which is a process known as evanescent-wave coupling. This could be accomplished by placing two optical waveguides in proximity with each other so that the evanescent field generated by one waveguide can transfer to the other waveguide without much decay[42].

In order to utilise the evanescent field for sensing applications, the core and the cladding diameters have to be reduced to obtain stronger evanescent field. The process of tapering can successfully reduce both of the diameters of the core and cladding, so that a larger fraction of power of guided mode will propagate in cladding as evanescent field. Although in the taper region the modes are not single modes as the untapered region for single mode fibre (SMF 28), the fundamental mode can still propagate without suffering much loss, as discussed in Chapter 2.

In this chapter, we demonstrate an evanescent wave coupling experiment by twisting two identical tapers for several turns. Twisting of the tapers provide tighter interaction length during the coupling via evanescence. By altering the twist angle, the contact distance between the tapers will be changed therefore different ratios of power division can be achieved. Then a thin film is coated on tapers by using the methods mentioned in Chapter 4, the purpose of which is to protect the fragile tapers as well as controlling the separation distance of the tapers, which determined the coupling efficiency.

5.2 Theoretical analysis of twisted fibres

The structure of a composite waveguide is illustrated Figure 5.1. It consists of two identical, step-profiled and single mode fibres of core radius ρ and centre-to-centre separation d. The refractive index of each core $n_{co} = n_{silica}$, and $n_{cl} = n_{air}$ in the surrounding medium.

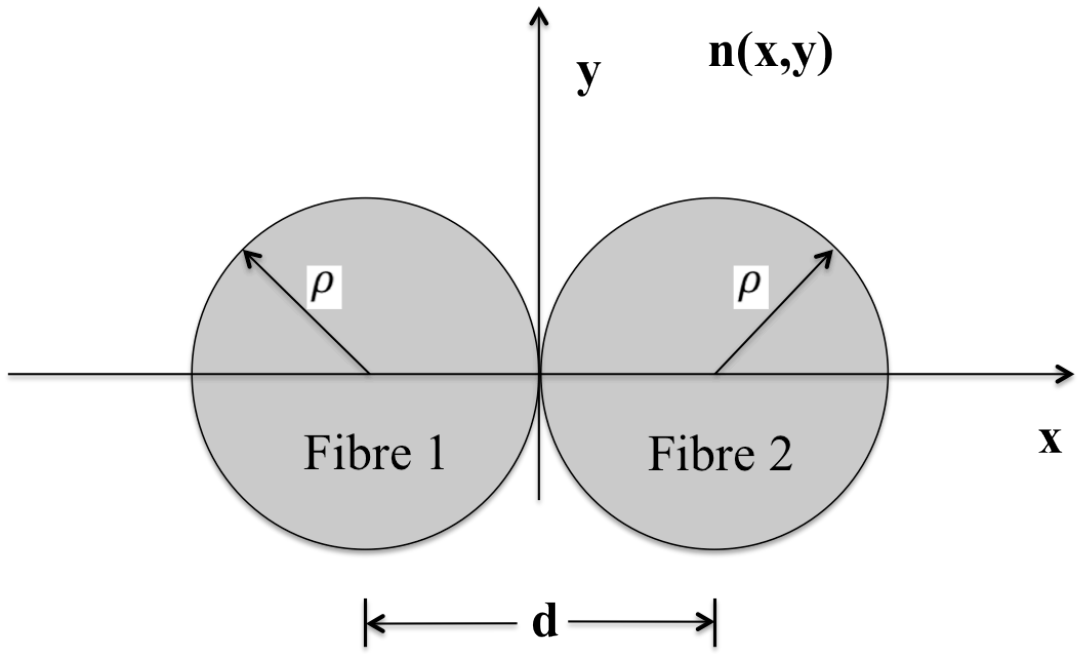

Fig 5.1 Cross-section of the composite waveguide comprises two fibres of core radii ρ with refractive index profile $n(x, y)$ and separation $d = 2\rho$

Based on the perturbation theory for the scalar waveguide, we can approximately derive accurate expressions for the modes of the perturbed fibre in terms of the known modes of the unperturbed fibre. The perturbed fibre is characterised by a refractive-index profile $n(x, y)$ relative to Cartesian axes in the cross-section [42].

In isolation, the unperturbed fibre 1 has refractive-index profile $n_1(x, y)$ and scalar wave equation solution $\Psi_1(x, y)$, as shown in Fig 5.2. The corresponding quantities for the perturbing fibre are $n_2(x, y)$ and $\Psi_2(x, y)$. By assumption $P_1(0) = 1$ and $P_1(0) = 0$, we deduce

$$P_1(z) = cos^2(Cz), P_2(z) = sin^2(Cz) \quad (5\text{-}1)$$

Hence, we need to calculate the coupling coefficient and total interaction length.

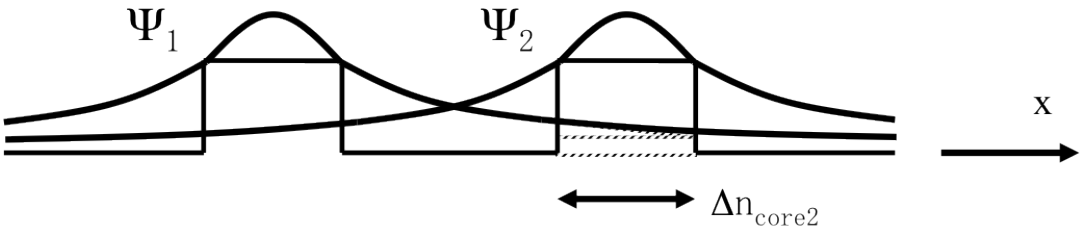

Fig 5.2 Mode fields of the composite waveguide where Ψ_1 is the mode field of fibre 1 and Ψ_2 is the mode field of fibre 2. Δn_{core2} is the overlap of Ψ_1 in the core of fibre 2 [43].

5.2.1 Coupling coefficient

The coupling efficiency can be approximated by [42]

$$C = k \int \Delta n_{core2}(x,y)\Psi_1(x,y)\,\Psi_2(x,y)dxdy \quad (5\text{-}2)$$

where $\Delta n_{core2} = n_2(x,y) - n_{cladding}$, and it is vanished over the core of the unperturbed fibre. To calculate C, we note that Δn_{core2} is non-zero only over the core of the second fibre, the approximate form is induced as [42]

$$C = \frac{(2\Delta)^{1/2}}{\rho}\frac{U^2}{V^3}\frac{K_0(Wd/\rho)}{K_1^2(W)} \cong \{\frac{\pi\Delta}{Wd\rho}\}^{1/2}\frac{U^2}{V^3}\frac{exp(-Wd/\rho)}{K_1^2(W)} \quad (5\text{-}3)$$

where $\Delta = \frac{n_{co}-n_{cl}}{n_{co}}$, $d = 2\rho$ as these cores are in proximity with each other, $V = k_0\rho(n_{co}^2 - n_{cl}^2)^{\frac{1}{2}}$, $U = \sqrt{(k_0^2n_1^2 - \beta^2)}\rho$, $W = \sqrt{(\beta^2 - k_0^2n_2^2)}\rho$, and K_1 is modified Bessel functions.

5.2.2 Total interaction length

The schematic of multi-twisted fibres is shown in Fig 5.3. Two fibres form a helix when intertwined and a derivation can be formulated for the length of contact distance corresponding to a given rotation angle Θ. Also, we assume that the angle of the helix pitch is ϕ.

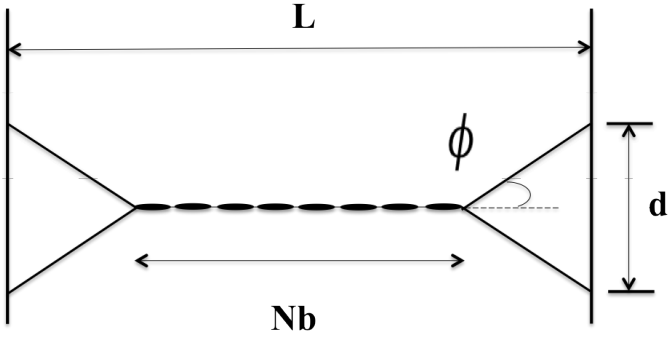

Fig 5.3 Schematic of multi-twisted fibre: N stands for the number of pitches, b is length of a single pitch of the helix, L represents the distance between stages, ϕ is the pitch angle and d is the spacing between two fibres.

From Fig 5.4 (a), we deduce $tan\phi = \frac{d}{L-Nb}$ so that

$$L = dcot\phi + Nb \tag{5-4}$$

while in the helix, for one pitch from Fig 5.4 (b), we obtain contact length for a single pitch

$$x = \sqrt{(2\pi\rho)^2 + b^2} \tag{5-5}$$

$$cot\phi = b/2\rho \tag{5-6}$$

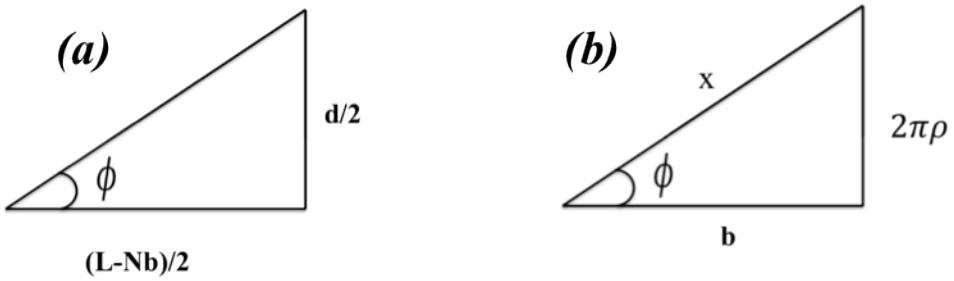

Fig 5.4 (a) A triangle simplified near a stage. (b) A schematic of the calculation of the length of helix around a fibre with a radius of ρ.

By substituting Eq. (5-6) into Eq. (5-4), we obtain that

$$L = d \cdot \frac{b}{2\pi\rho} + Nb = (\frac{d}{2\pi\rho} + N)b \tag{5-7}$$

The values of these variables are all known expect for b, thus $b = L/(\frac{d}{2\pi\rho} + N)$.

So the total contact length is given by:

$$z = N \cdot x = N\sqrt{(2\pi\rho)^2 + b^2} \tag{5-8}$$

where $N = \frac{Angle\ of\ turn}{360^\circ} - 0.5$.

5.3 Experimental design of evanescent-wave coupling

Experimental design is of great importance as the tapers are microstructures that require precise control in use.

On the base of the taper rig, the distance between two fibres was designed to be separated by 0.3mm, as shown in Fig5.5 (a). The fibres were clamped tightly to taper the two fibres at the same time. Fig 5.5(b) was the photo of the designed holder, which was fixed in the taper rig to stabilise two fibres with 0.3mm separation distance.

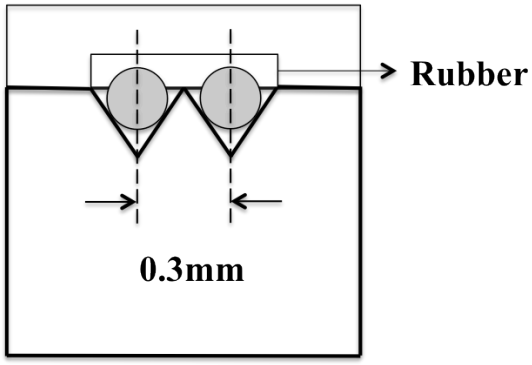

(a)

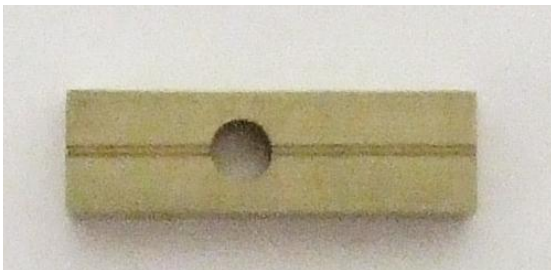

(b)

Fig 5.5 (a) Cross-section of designed holder for two fibres with a separation distance of 0.3mm. (b) A photo of a designed holder that stabilises two fibres (right).

Another import part of the experiment is the rotation stage, which controls the rotation angle of two twisted fibres, as shown in Fig 5.6. An important element of the design is that the height of fibres must be in the centre of the rotation stage, as the result no bend loss will be produced when fibres are twisted. Holes drilled on the stages are circled in Fig 5.6. These holes are intended to clamp the stage and to maintain the same distance of the stages for the coupling of the tapers. Separation distance of the stages could be locked.

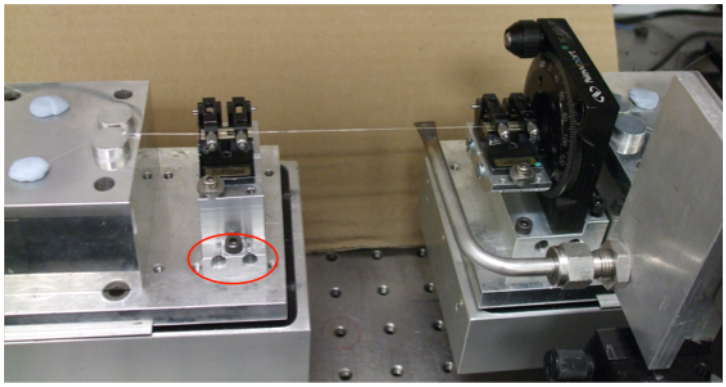

Fig 5.6 Rotation stage and the tapering setup

Fig 5.7 shows the experimental setup as well as the tapering system and measure system. The first stage of the experiment was to fabricate two identical tapers simultaneously with a taper rig, and then a light source (1550nm) was coupled into one end of the fibre and lastly the fibres were twisted with the rotation stage. The output power and coupled power were measured with an optical multimeter. During

the procedures, the coupling property of the tapers can be viewed through a microscope and projected on a monitor.

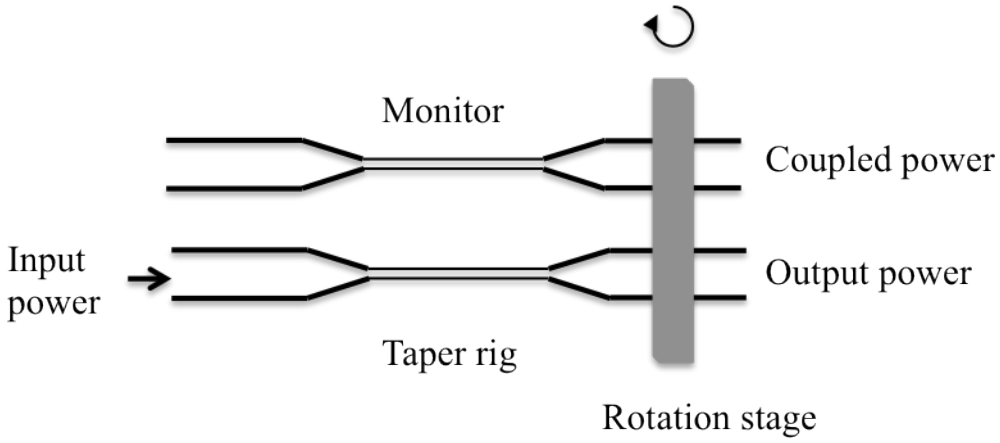

Fig 5.7 A schematic of coupling experimental setup

5.4 Experimental procedure

Before tapering, the region of the fibres that is supposed to be processed were stripped of coating and cleaned with acetone. The fibres must be clamped extremely tight to prevent them from slipping away when the stages were pulling apart. The entire setup was connected to an optical multimeter so that the loss during tapering could be measured. The tapering process was controlled by a computer program with the settings of 5μm diameters of two fibres and 1cm taper waist respectively. During the tapering process, the position of the flame must be corrected since both of the fibres were required to be stretched to the equal thickness. The distance between the stages was measured to be 7.5cm after tapering process.

At the beginning, both of the optical detectors were connected to the ends of two tapers to measure the total power before twisting. The data were used to normalise the intensity, which could reduce the influence of the different intrinsic errors of two different detectors. Followed by twisting one end of the fibres in an interval 30° from

0° up to 1440°, the data were continually collected to observe the power transfer.

5.5 Results and discussion

The stability of the coupling process was examined by twisting and untwisting the fibres to pursue the stability over time. To test the repeatability of the experimental procedure, many experiments based on the same procedure have been done. Here we list two figures (Fig 5.8 and Fig 5.9) that represent two different experiments of twisted tapers (denoted as group 1 and group 2) with parameters that supposed to be the same. Both graphs contain two diagrams, where Fig 5.8(a) and Fig 5.9(a) represent the data that was collected at the beginning when twisting the tapers, while the data in Fig 5.8(b) and Fig 5.9(b) was collected after twisting and untwisting of the fibres for three times.

Normalised intensity is essential to eliminate the difference of two detectors. Firstly, the initial total power was collected by two detectors as P_{10} and P_{20} respectively. Then during the twisting, the measuring data were divided by each tested initial powers to obtain a normalised power. Periodic variation of the normalised intensity with rotated angle can be seen in all these figures demonstrated in Fig 5.8 and Fig 5.9. The measured period cycles of group 1 and 2 were 150° and 180°, respectively. The results were not exactly the same in periodicity, which may due to the potential difference in different tapers. The minimum normalised intensity was approaching zero and the maximum point is approximately 1, which indicated that the coupling was symmetric. After twisting and untwisting for three times, the maximum power became lower than that obtained earlier. This loss was perhaps caused by the contamination, such as dust from the air falling over the tapers.

Additionally, the collected data might suffer some errors due to the fluctuations in the display of optical multimeter. However, it was quite strange that at some point the power exceeds 1. The reason is still unknown; one of the possible explanations is that

the position of fibres might have moved slightly, thus some extra power could be probably coupled into the detectors.

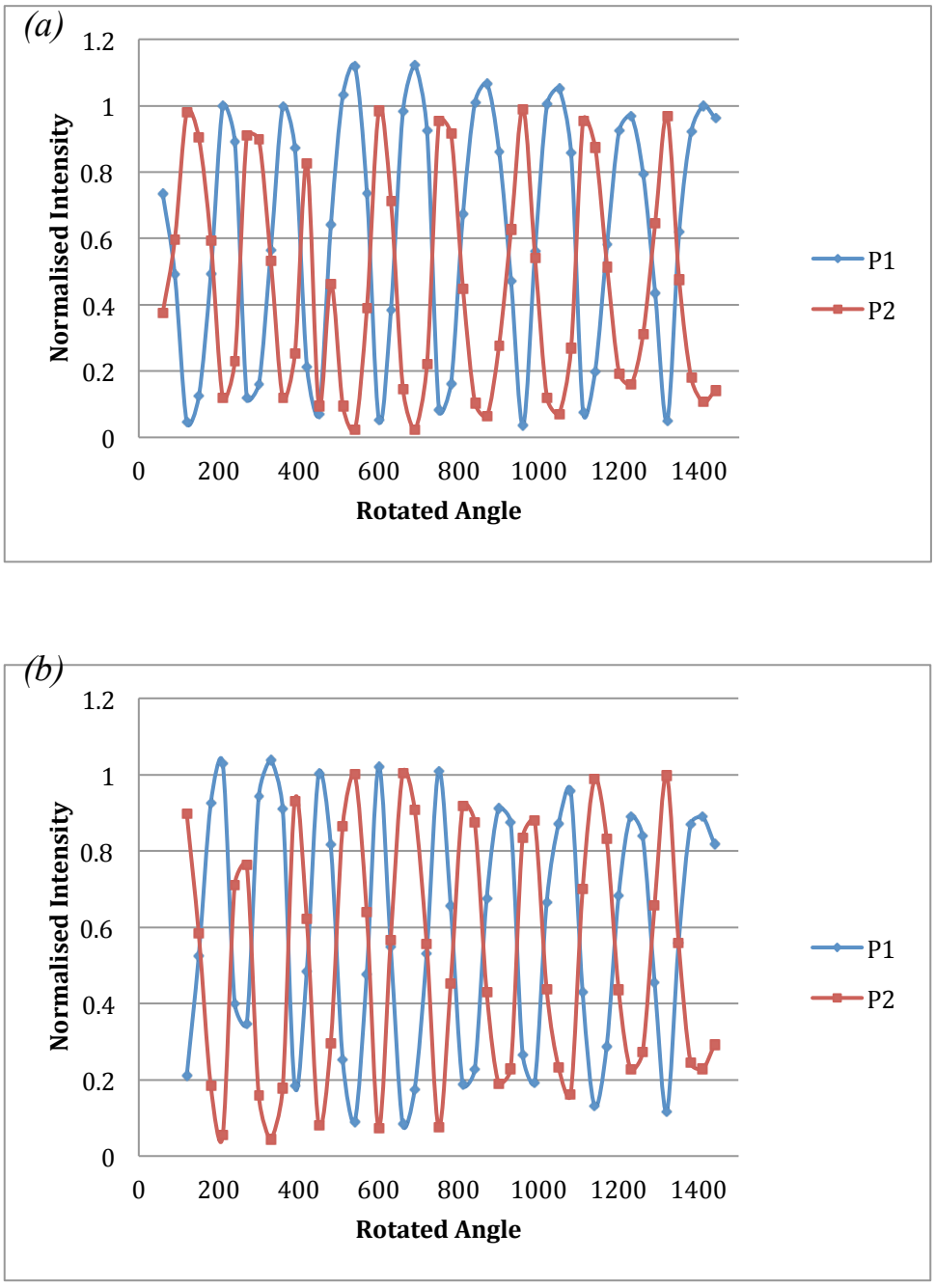

Fig 5.8 Relationship of rotated angle and normalised intensity of twisted fibres (group 1) after: (a) twisting once and (b) twisting and untwisting three times

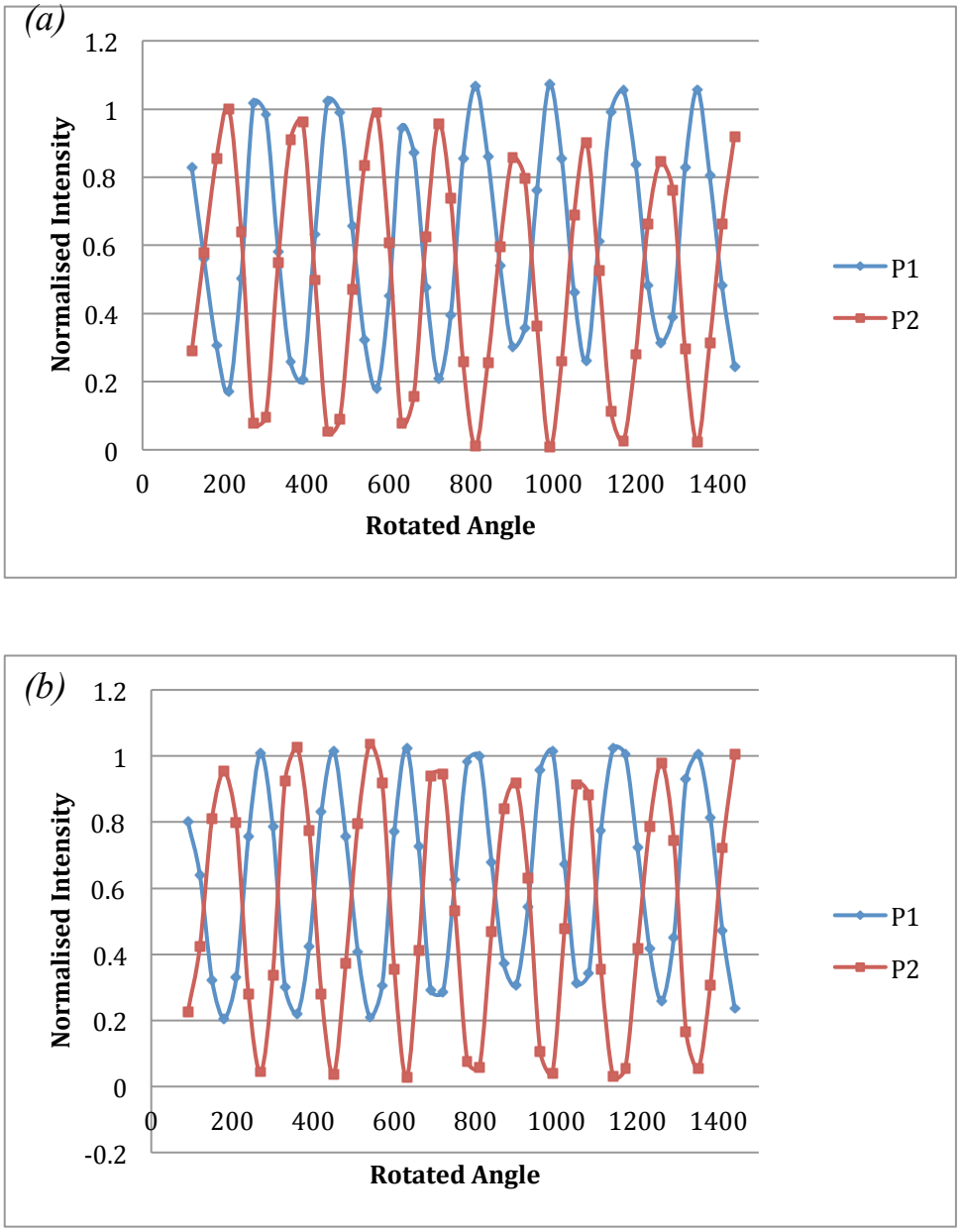

Fig 5.9 Relationship of rotated angle and normalised intensity of twisted fibres (group 2) after: (a) twisting once and (b) twisting and untwisting three times

As described in the experimental procedure, the total interaction length can be recorded through a CCD camera that was connected to a monitor. Fig 5.10 shows the twisting waist on a monitor and interaction length was measured to be approximately 1.4cm with the help of a scale.

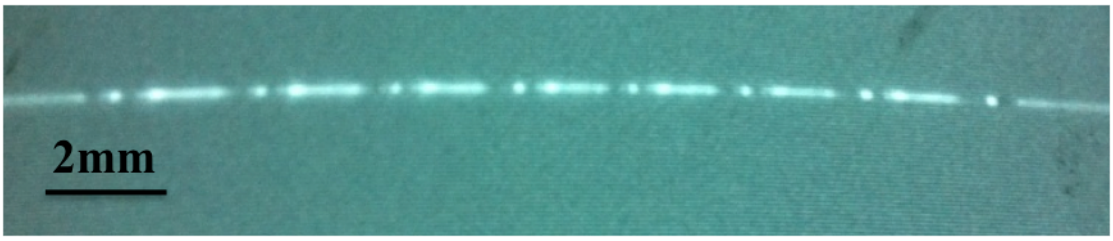

Fig 5.10 A photo of the interaction length of twisted tapers on TV screen

From Eq. (5-10) the calculated interaction length is 1.16cm with L=7.5cm, d=0.3mm, N=3.5, $\rho = 2.5\mu m$. The theoretical graph is shown in Fig 5.11 where the analysed period cycle is calculated to be a 155°. Since the experiment conditions was not perfect, the experimental results of period cycle of 150° and 180° in Fig 5.8 and Fig 5.9, respectively, suggests the practical results were obtained in correspondence with the theoretical analysis within experimental error.

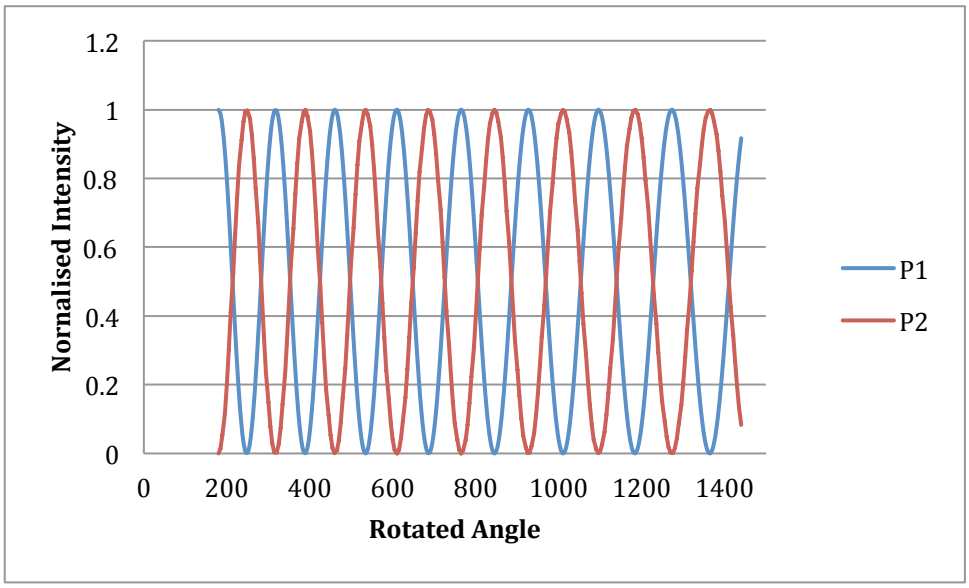

Fig 5.11 Theoretical relationship of normalised intensity versus rotation angle

To summarise, for the same pair of tapers, little change occurred to the periodicity of the normalised intensity when they were twisted once and were twisted and untwisted three times. The coupling stability lasted at least 5 hours. In these experiments, the periodicity varied slightly from time to time but was still approximately the same. However, if the coating could contribute to a much greater difference, then a couple

of tapers could have been used as control experiments.

5.6 Taper with thin film coating

In this part, the process the crack-free film deposition process described in Chapter 4 was used to treat smaller diameter tapers (5μm). This required more precise control since the needle may break the taper during the translation. Followed by the coating process, the film deposited on tapers were aged in methanol atmosphere and then used in the twisted coupling experiment.

5.6.1 Loss analysis

Transmission loss was considered since it would significantly affect the evanescent wave coupling experiment. Cutback technique was used to measure the loss of a thin film coated taper as shown in Fig 5.12. It begins by measuring the output power $P_y$of the test taper with coated film with an optical multimeter, then without disturbing the input conditions, the test taper coated with film was cut and the output power was measured as P_x, then the loss was given by [29]

$$dB = -10log\ (\frac{P_y}{P_x}) \qquad 5\text{-}11$$

After stretching from the taper rig, the tapers were coated with sol-gel using the process demonstrated in Chapter 4 for the crack-free film, and then aging in methanol atmosphere for 12hrs. Then a 1550nm laser was used to launch the light into one end of the taper and stored the data by a optical multimeter. After that, the taper part was cut, as shown in Fig 5.12 (dashed line) and the power of the shorter piece of fibre was measured. According to the Equation (5-11), the loss of a 5μm diameter taper with thin film coating was calculated to be 0.7~1.0dB at 1550nm.

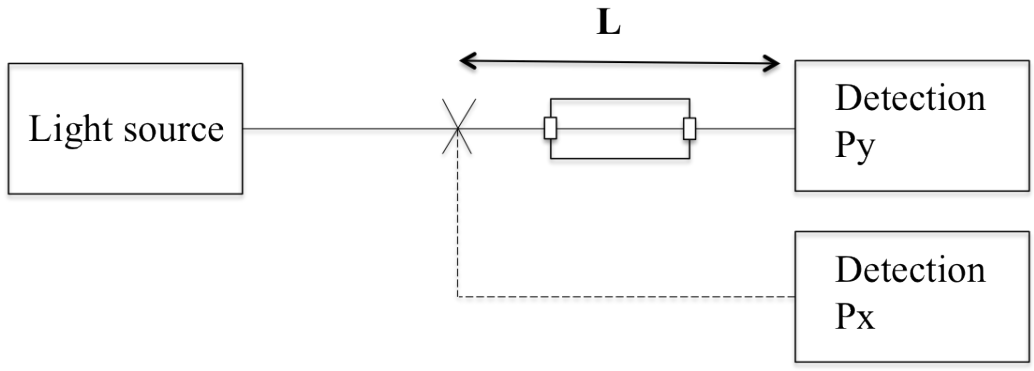

Fig 5. 12 A schematic of the cutback measurement.

5.6.2 Twisted tapers with coatings

Same bare fibres were used in the coupler experiments with coated and uncoated fibres for comparison. Firstly two tapers were place in proximity and a drop of sol suspended at the needle tip was translated to conduct the dip coating. However, since the diameter of the drop was 0.5mm, which was larger than tapers spacing of 0.3mm and the surface tension and adhesion was not strong enough to separate the drop into two droplets, it was observed that the coating was all over as well as in between both fibres instead of having coatings separately on each fibre, as illustrated in Fig 5.13.

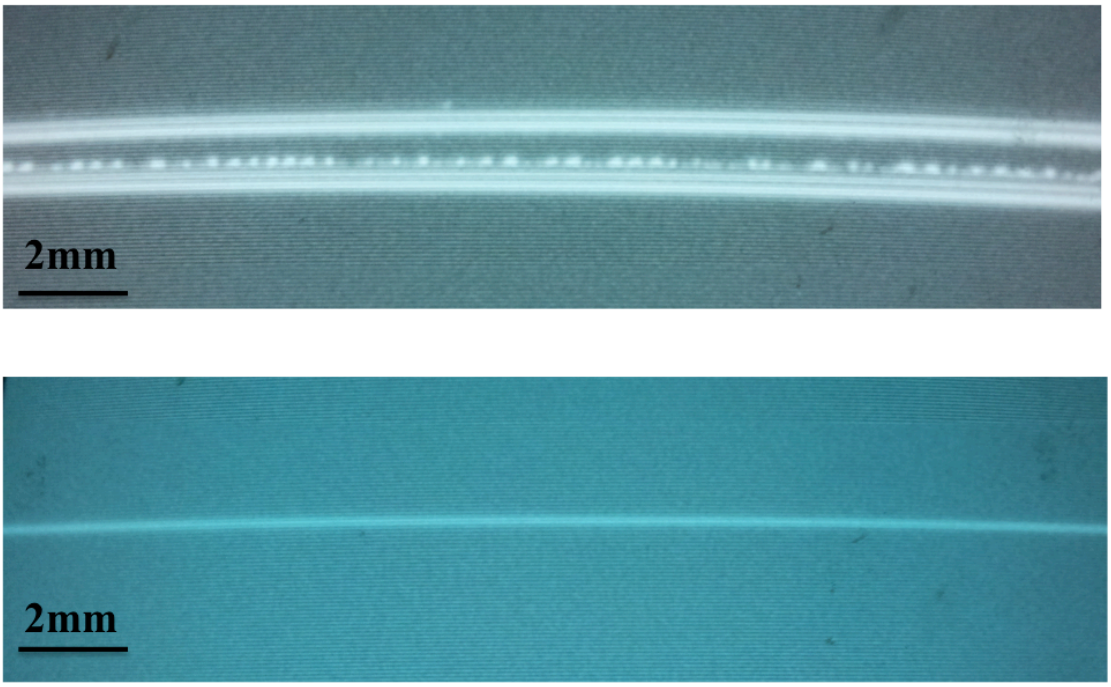

Fig 5.13 Pictures of two separated tapters after coating: untapered regions (top) and tapered regions (bottom). The bright dots in the top picture indicated the gel was formed on the fibre while the bright thin line in the bottom picture indicated the taper waists were merged together after coating.

In such case, four tapers had to be used in the coupling experiments: two bare tapers coupled acted as control experiment, while other two tapers were separately coated with a thin layer of films and then used in the experiments of evanescence wave coupling.

As described above, in order to obtain two well coated thin films on the taper without contaminating the surface, two separated tapers have to be separately coated and recombined with the twisting clamp.

Fig 5.14 demonstrates the idea of the three steps that bring the two tapers (5μm) to a 0.3mm spacing. The first step requires the level of the mount base to be precisely adjusted as the tilt-induced stress will break the taper if the heights of fibres are not in parallel with each other. The second step needs a removable base (red) that helps the holder separate away from the mount without stretching the brittle tapers (Fig 5.14 (b)). The final step is to bring the tapered fibre that is fixed in the second step into the coupling stage and to carefully place the two coated tapers in the correct position.

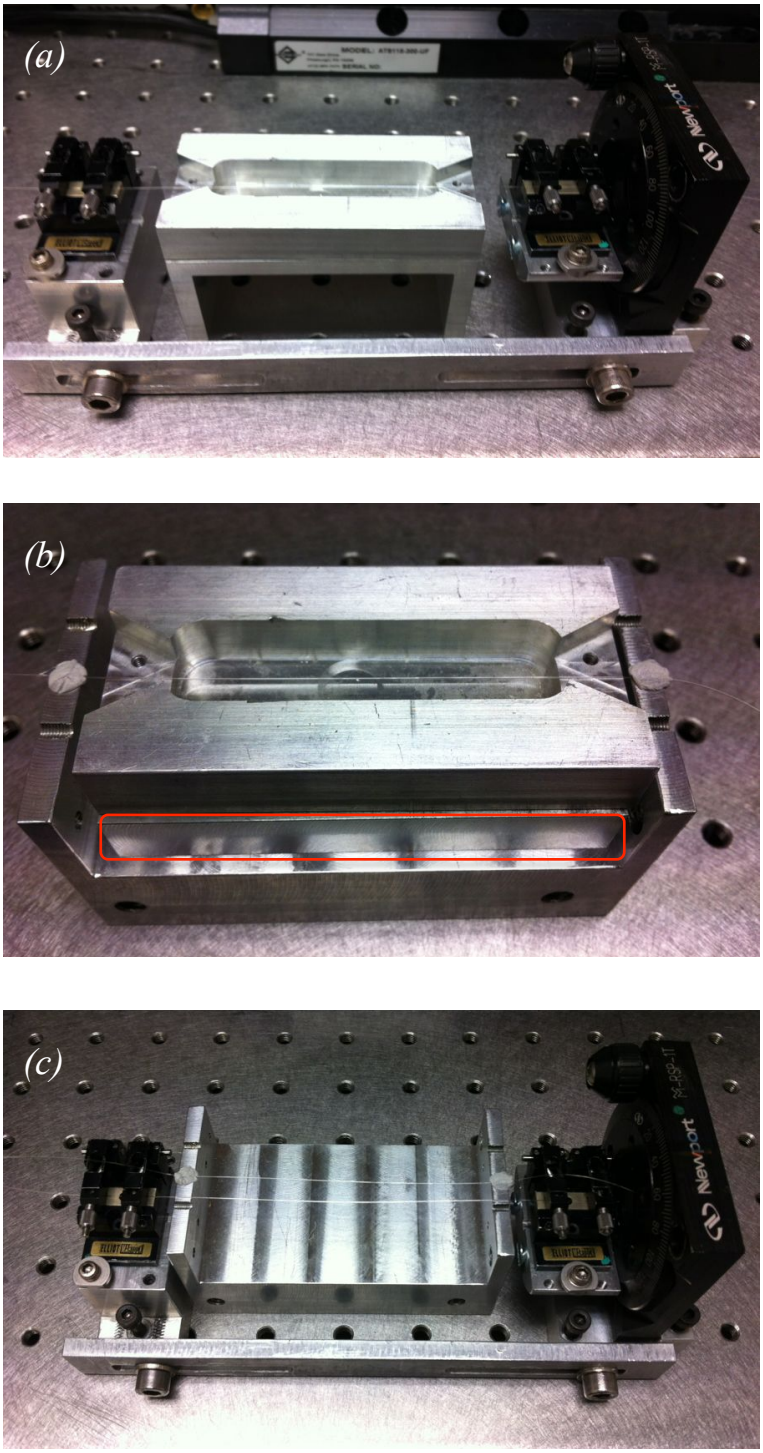

Fig 5. 14 Three steps of bringing two coated tapers in proximity of a 0.3mm distance

So far, in practice, the coupling experiment was not easily completed with 5μm diameter tapers since they were so fragile. However, 6.6μm diameter tapers could be more promising if handled with care in the procedure, especially the last step that required a subtle control of the tension to straighten the tapers and to ensure that the

tapered regions were in the middle of the stages. Fig 5.15 shows the 6.6μm tapers with a 2cm taper waist. It was designed to increase the possibility of coupling in the centre of the stages at 11.5cm, which would fit the holders while allow flexible movement of the tapers. Though the practical results of coupling between two uncoated tapers with diameters of 6.6μm, as seen in Fig 5.15 (b), was not in a good agreement with the theoretical analysis (Fig 5.15(a)) compared to that of 5μm tapers coupling, which can been seen from Fig 5.8 and Fig5.11, it still indicated that the period cycle became larger when the separation distance became larger. However, the irregular correlation evanescent-wave coupling of tapers with coating requires further investigation.

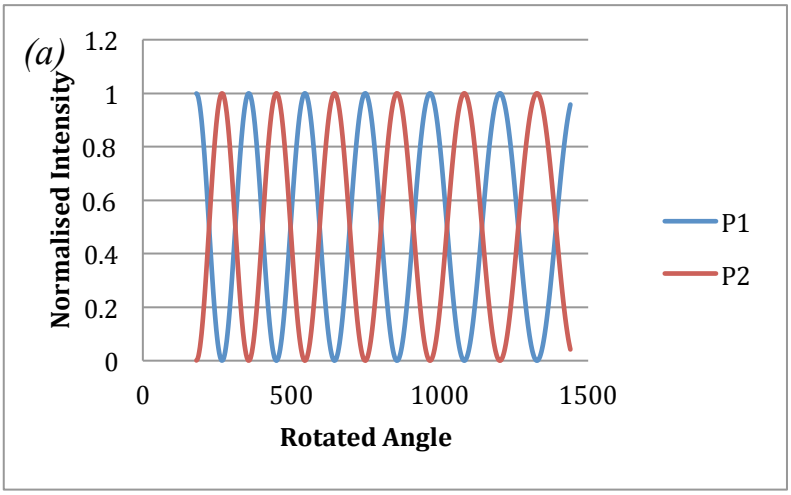

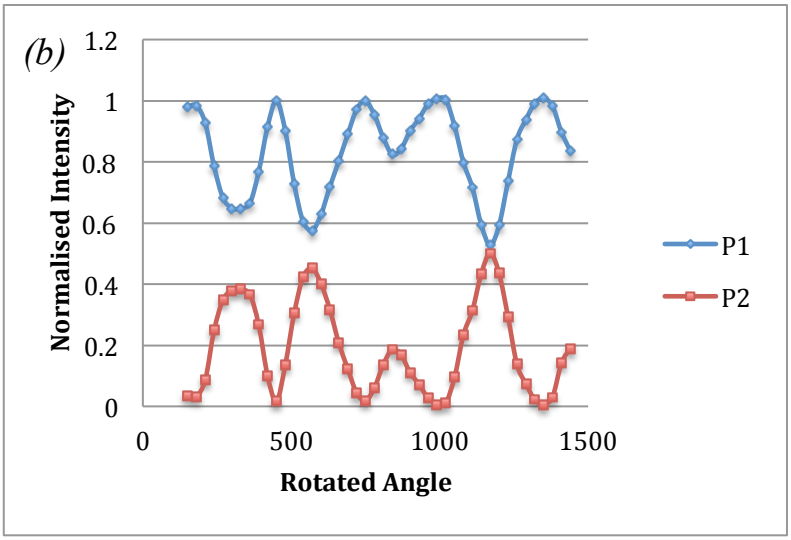

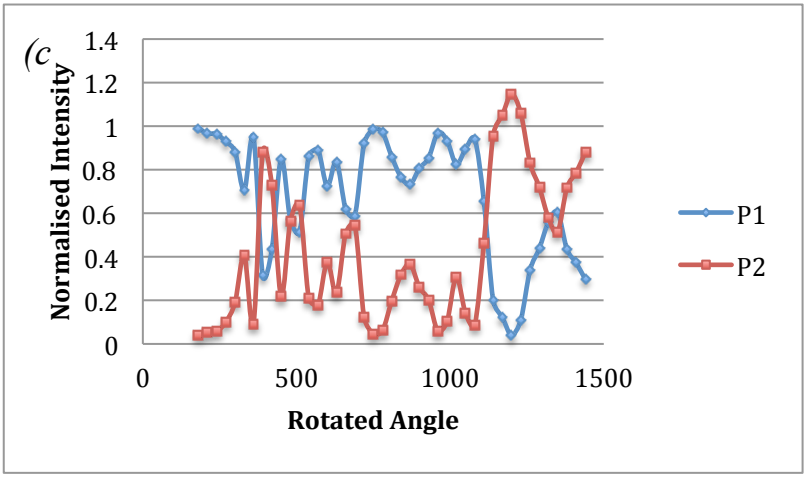

Fig 5.15 (a) Theoretical analysis of twisting tapers with diameter of 6.6μm and (b) Experimental results of twisting tapers with diameter of 6.6μm ;(c) Experimental results of twisting tapers with diameter of 6.6μm after sol-gel coating procee.

5.7 Conclusion

An initial design of evanescent wave coupling experiment had been illustrated. Repeatable test results of coupling between two tapers with 5μm diameters with separation of 0.3mm from a 7.5cm-long stage had been conducted to confirm the stability of the experimental equipment. The loss of tapers with thin film coating had been found to be about 0.7~1.0dB. Efforts had been made that may assist evanescent wave coupling between tapers with coating.

Chapter 6 Conclusions

This thesis covered the application of sol-gel process in fibre optics. The sol-gel procedure of making aerogel and xerogel was discussed in detail and experiments of fibre with aerogel core and thin film around fibre were presented.

6.1 Summary of results

To understand the influence of the aerogel filled fibre on the light guided in the core, an aerogel waveguide was fabricated inside a selectively filled hollow core fibre, which protected the aerogel and provided a low-index cladding that guided light by total internal reflection over a range of wavelengths over 584.7nm. The proposed fibre was filled using a vacuum pump initially and the results indicated that the light was confined in the core and became brighter when the wavelength moved into the infrared area, which satisfied the design purpose.

To further investigate the filling situation, index-matching fluid was injected into the filled aerogel fibre. Gaps between the aerogel sections occurred in the filled aerogel core, which might be caused by bubbles dissolved in sol or the uneven gelling time driven by the vacuum pump. Thus, an improved method known as positive pressure filling was proposed and tested. It has unparalleled advantages: time consumption was reduced because it could create a larger filling pressure difference and the drop that came out of the fibre outlet could be directly observed with a microscope.

As for the fabrication of silica thin film as a potential packing material to protect fragile tapers in the future, we have developed a method to deposit silica thin film on the surface of fibres without cracking. The gelling time of selected sol was found to be about 10 min. By dividing the process into different coating times and aging times, the optimal experimental procedures and methods were discovered. Silica films produced in this way were crack-free; however, they were hydrophilic and hence were

very likely to be destroyed by water. Two different methods were proposed to improve the hydrophobicity of these thin films: the experimental results illustrated that washing in HMDS contributed a much larger contact angle than using MTMS as a co-precursor for thin films.

The physical properties of these silica films such as thickness, microstructure and refractive index were characterised by SEM, TEM and ellipsometer, respectively. The cross-section SEM photo of optical fibre coated with silica thin film suggested the thickness of deposited film was of 600nm approximately, while inspection of the tiny flakes collected from scratching the surface of coated fibre under TEM revealed a less open network structure and a denser silica concentration compared to that of aerogel that was fabricated using the same recipe. Direct refractive index measurement of the cylindrical silica was quite difficult; to make the ellipsometric measurement operational the same fabrication process was done on a flat silica substrate and the refractive index was found to be 1.30. Though the measured refractive index might not be the exactly refractive index of the film coated on the fibre, this method still presents an approach for thin silica films deposited in such way.

A potential application of silica film coated on fibres was evanescent wave coupling. Since coupling efficiency was strongly affected by the spacing of two tapers, coating with multiple layers of thin silica film would definitely alter the spacing as well as the coupling efficiency. Initial design of evanescent wave coupling experiment was illustrated and results of coupling between two tapers with 5μm diameters with a separation distance of 0.3mm from a 7.5cm-long stage corresponded with the theory. The loss of tapers with thin film coating was measured to be about 0.7~1.0dB. As for the next stage of comparing the two coupling efficiencies between tapers with and without thin silica films, a proposed experimental setup was designed.

6.2 Future work

This thesis presented the integration of sol-gel process with fibre optic using two technologies, namely the aerogel filled hollow core fibre and the coating of thin silica film on tapers.

The most obvious future experiments involve combining doped aerogel with our techniques for the fabrication of waveguides based on doped aerogel in the fibre core. It was reported that aerogel has been successfully doped with gold nano-particles, nano diamonds, rare earth ions, laser dyes, inorganic and organic molecules and other nano-particles [44], and there are more to explore. This should not be technologically challenging, as the methods and equipment for such experiments have already been developed. Only then would we be ready to investigate this type of aerogel as the core of a waveguide, possibly with the view of additional properties with an aerogel core.

Silica film developed on optical fibres may become aerogel through "spring back" effect after an accurate drying process [45]. Therefore coating the tapered fibre with aerogel films could help extend their potential applications due to its low refractive index. Since aerogels do not influence the light guiding, comparative experiments between two taper couplers and two tapers packed in aerogel thin films will demonstrate the influence of coupling efficiencies because aerogel films separate the spacing between tapers in a better way. Alternatively, thicker aerogel or xerogel films of a few hundred microns will greatly reduce the response time of gas sensors. It has already been reported that, through measuring the change in fluorescence of a doped aerogel, an effective oxygen sensor can be made [46].

In all, the further study combining sol-gel process and fibre optics may lead to more exciting applications in industry.

References

[1] Buckley, A. and M. Greenblatt, *The sol-gel preparation of silica gels.* Journal of chemical education, 1994. **71**(7): p. 599.

[2]Grote, N.and H. Venghaus, *fibre optical commination devices*, 2001 Springer-Verlag Berlin Heidelberg New York

[3] Klein, L.C., *Sol gel optics: Processing and applications*, 1994. Springer-Verlag US

[4] Brinker, C.J. and G.W. Scherer, *Sol-gel science: the physics and chemistry of sol-gel processing*1990: Academic Pr.

[5] Pierre, A.C. and G.M. Pajonk, *Chemistry of aerogels and their applications.* Chemical Reviews-Columbus, 2002. **102**(11): p. 4243-4266.

[6] Grogan, M.D.W., et al., *Silica aerogel core waveguide.* Optics Express, 2010. **18**(21): p. 22497-22502.

[7] Birks, T.A. and Y.W. Li, *The shape of fiber tapers.* Lightwave Technology, Journal of, 1992. **10**(4): p. 432-438.

[8] Hosticka, B., et al., *Gas flow through aerogels.* Journal of Non-Crystalline Solids, 1998. **225**: p. 293-297.

[9] Xiao, L., et al., *Tapered fibers embedded in silica aerogel.* Optics letters, 2009. **34**(18): p. 2724-2726.

[10] Hurd, A.J. and S.M. Rao, *Silica aerogel films prepared at ambient pressure by using surface derivatization to induce reversible drying shrinkage.* Nature, 1995. **374**: p. 439.

[11] Hong J.K, Yang H.S, *Preparation ans characterization of porous silica xerogel film for low dielectric applicaion,* Thin solid films, 1997. **308-309**:p495-500

[12] Kakarantzas, G., T. Birks, and P.S.J. Russell, *Low-loss deposition of solgel-derived silica films on tapered fibers.* Optics letters, 2004. **29**(7): p. 694-696.

[13] Kistler, S., *Coherent Expanded Aerogels and Jellies.* Nature, 1931. **127**: p. 741.

[14]Grogan, M., *Aerogel and Fibre Optics*, 2010, Bath

[15] Kralchevsky, P.A. capillary forces between colloidal particles, Langmuir 1994.**10**(1): p.23-36

[16] Hurd, A.J. and S.M. Rao, *Silica aerogel films prepared at ambient pressure by using surface derivatization to induce reversible drying shrinkage.* Nature, 1995. **374**: p. 439.

[17] Soleimani Dorcheh, A. and M. Abbasi, *Silica aerogel; synthesis, properties and characterization.* Journal of materials processing technology, 2008. **199**(1-3): p. 10-26.

[18] Jet Propulsion Laboratory, C.I.o.T., *Aerogel-catching comet dust*, in *http://stardust.jpl.nasa.gov/photo/aerogel.html*, N.J.A.-c.c. dust, Editor 2009.

[19] Hunt A.J., *Light of scattering of aerogel characterisation,* Journal of Non-Crystalline Solids,1988 **225** p:303-305

[20]Gulrez, K. H, Saphwan A.A, Phillips, G. O, *Hydrogels: Methods of Preparation, Characterisation and Applications*, Progress in Molecular and Environmental Bioengineering 2011 **5** p. 118-149

[21] Leventis, N, I.A Elder, etal, *Durable Modification of Silica Aerogel Monoliths with Fluorescent 2,7-Diazapyrenium Moieties. Sensing Oxygen near the Speed of Open-Air Diffusion* N Materials, Chemistry of1999 **11** (10), pp 2837–2845

[22] Crisp, J. and B. Elliott, *Introduction to fiber optics*2005: Elsevier.

[23] Hrubesh, L.W., *Aerogel applications.* Journal of Non-Crystalline Solids, 1998. **225**: p. 335-342.

[24] Richter, D. and D. Lipka, *Measurement of the refractive index of silica aerogel in vacuum.* Nuclear Instruments and Methods in Physics Research Section A: Accelerators, Spectrometers, Detectors and Associated Equipment, 2003. **513**(3): p. 635-638.

[25] Brinker, C., *Hydrolysis and condensation of silicates: effects on structure.* Journal of Non-Crystalline Solids, 1988. **100**(1-3): p. 31-50.

[26] Rassy. H. E and AC Pierre, *NMR and IR spectroscopy of silica aerogels with different hydrophobic characteristics,* Journal of non-crystalline solids, 2005. **351** (19-20) .p :1603-1610

[27] Yokogawa, H. and M. Yokoyama, *Hydrophobic silica aerogels.* Journal of Non-Crystalline Solids, 1995. **186**: p. 23-29.

[29] Buck, J.A., *Fundamentals of optical fibers*2004: Wiley-Interscience.

[30] Tsao, C. Optical waveguide analysis 1991: Oxford University Press

[31]Birks, T.A., *"Fibre transitions and tapering "*, in *http://www.bath.ac.uk/physics/groups/cppm/tapers.php*, URL, Editor 2010.

[32] Love, J., et al. *Tapered single-mode fibres and devices. I. Adiabaticity criteria*. 1991. IET.

[33] Birks T.A, Russell P.S.J., Culverhouse D.O, *The acousto-optic effect in single mode fiber tapers and couplers*. Lightwave Technology, Journal of,, 1996. **14**(11): p. 2519 - 2529

[34] Wang, C. C.Wu, et al *Humidity sensors based on silica nanoparticle aerogel thin films*. Sensors and Actuators B:Chemical, 2005. **107**:p. 402-410

[35]Hong JK, Kim HR, Park H H, *The effect of sol viscosity on the sol–gel derived low density SiO_2 xerogel film for intermetal dielectric application,* Thin solid films 1998. **332**(2):p. 449-454

[36] Hrubesh, L.W. and J.F. Poco, *Thin aerogel films for optical, thermal, acoustic and electronic applications.* Journal of non-crystalline solids, 1995. **188**(1-2): p. 46-53.

[37] Robert N. Wenzel, *Surface Roughness and Contact Angle* Journal of Physical Chemistry., 1949, **53** (9): p.1466–1467

[38]H Todokoro, M Ezumi, *Scanning electron microscope* US Patent 5,872,358, 1999

[39] David B. Williams, C. Barry Carter, *The Transmission Electron Microscope* 1996 Springer-Verlag US

[40] Azzam, R.M.A.; Bashara, N.M. , *Ellipsometry and polarized light*,1987. Amsterdam and New York: New York

[41] en.wikipedia.org, 2013, 06

[42] Snyder, A.W. and Love, J.D., Optical waveguide theory, IBT Global, London, 2000

[43] Prof. Tim Birks' presentation of "modes".

[44] RW Pekala, R. W, J.C. Farmer, etl, *Carbon aerogels for electrochemical applications* Journal of Non-Crystalline Solids, 2004. 225. p: 74-80

[45] Hurd, A.J. and S.M. Rao, *Silica aerogel films prepared at ambient pressure by using surface derivatization to induce reversible drying shrinkage.* Nature, 1995. **374**: p. 439.

[46] Plata, D.L., et al., *Aerogel-platform optical sensors for oxygen gas.* Journal of Non-Crystalline Solids, 2004. **350**: p. 326-335.

Appendix

Table of value of V, U, W, K1, ρ and coupling coeffiecentict C

V	U	W	$K_1(W)$	ρ	C
3	1.914706	2.309539	0.093842875	7.04829E-07	91099.82407
3.5	1.9809175	2.885475	0.046087193	8.22301E-07	61702.58986
4	2.0301471	3.4465204	0.023673398	9.39772E-07	42894.0987
4.5	2.068443	3.9964414	0.012534425	1.05724E-06	30657.0467
5	2.0992279	4.5379778	0.006781842	1.17472E-06	22484.27374
5.5	2.124597	5.0730748	0.003729031	1.29219E-06	16875.69519
6	2.1459128	5.6031293	0.00207607	1.40966E-06	12927.28575
6.5	2.1641051	6.1291638	0.001167238	1.52713E-06	10082.39003
7	2.1798328	6.6519418	0.000661503	1.6446E-06	7989.45707
7.5	2.1936774	7.1720442	0.000377354	1.76207E-06	6421.352362
8	2.2057004	7.6899211	0.000216444	1.87954E-06	5225.221195
8.5	2.2164785	8.2059261	0.000124726	1.99702E-06	4300.310895
9	2.226128	8.7203414	7.216E-05	2.11449E-06	3575.051358
9.5	2.2348202	9.2333948	4.18919E-05	2.23196E-06	2999.365569
10	2.2426931	9.7452721	2.43931E-05	2.34943E-06	2537.319772
10.5	2.2498589	10.256127	1.42414E-05	2.4669E-06	2162.720376
11	2.2564101	10.766086	8.33403E-06	2.58437E-06	1856.208031
11.5	2.2624233	11.275258	4.88723E-06	2.70184E-06	1603.270259
12	2.267963	11.783732	2.87133E-06	2.81932E-06	1392.915887
12.5	2.2730835	12.291586	1.68979E-06	2.93679E-06	1216.711071
13	2.2778311	12.798886	9.95971E-07	3.05426E-06	1068.126608
13.5	2.2822455	13.305689	5.87843E-07	3.17173E-06	942.0561363
14	2.2863608	13.812044	3.47397E-07	3.2892E-06	834.4719254
14.5	2.2902067	14.317994	2.05538E-07	3.40667E-06	742.1693342
15	2.2938091	14.823577	1.21737E-07	3.52415E-06	662.5789407
15.5	2.2971903	15.328826	7.21734E-08	3.64162E-06	593.6265848
16	2.3003705	15.833771	4.28278E-08	3.75909E-06	533.6253735
16.5	2.303367	16.338436	2.54355E-08	3.87656E-06	481.1978831
17	2.3061954	16.842846	1.5118E-08	3.99403E-06	435.2067872
17.5	2.3088696	17.347021	8.99213E-09	4.1115E-06	394.7130367
18	2.3114019	17.850978	5.35214E-09	4.22897E-06	358.9359108
18.5	2.3138033	18.354735	3.18763E-09	4.34645E-06	327.220308
19	2.3160838	18.858307	1.89962E-09	4.46392E-06	299.0168357
19.5	2.3182524	19.361707	1.13268E-09	4.58139E-06	273.8620553
20	2.3203171	19.864947	6.7574E-10	4.69886E-06	251.3629648